



HAL
open science

Carbon dioxide in silica-undersaturated melt Part I: The effect of mixed alkalis (K and Na) on CO₂ solubility and speciation

Yann Morizet, Michael Paris, Fabrice Gaillard, Bruno Scaillet

► **To cite this version:**

Yann Morizet, Michael Paris, Fabrice Gaillard, Bruno Scaillet. Carbon dioxide in silica-undersaturated melt Part I: The effect of mixed alkalis (K and Na) on CO₂ solubility and speciation. *Geochimica et Cosmochimica Acta*, 2014, 141, pp.45-61. 10.1016/j.gca.2014.06.014 . insu-01016894

HAL Id: insu-01016894

<https://insu.hal.science/insu-01016894>

Submitted on 2 Jul 2014

HAL is a multi-disciplinary open access archive for the deposit and dissemination of scientific research documents, whether they are published or not. The documents may come from teaching and research institutions in France or abroad, or from public or private research centers.

L'archive ouverte pluridisciplinaire **HAL**, est destinée au dépôt et à la diffusion de documents scientifiques de niveau recherche, publiés ou non, émanant des établissements d'enseignement et de recherche français ou étrangers, des laboratoires publics ou privés.

Carbon dioxide in silica-undersaturated melt Part I: The effect of mixed alkalis (K and Na) on CO₂ solubility and speciation.

Yann Morizet^{1,3*}, Michael Paris², Fabrice Gaillard³, Bruno Scaillet³

(1) Université de Nantes, Nantes Atlantique Universités, Laboratoire de Planétologie et Géodynamique de Nantes (LPGN)

UMR CNRS 6112

2 rue de la Houssinière, 44322 NANTES (France)

(2) Institut des Matériaux Jean Rouxel (IMN), Université de Nantes

UMR CNRS 6502

2 rue de la Houssinière, BP32229, 44322 NANTES Cedex 3 (France)

(3) CNRS – Université d'Orléans – BRGM

UMR 7327

Institut des Sciences de la Terre d'Orléans

1a rue de la Férollerie, 45071, Orléans, France

Corresponding author: Yann Morizet

Postal address:

Laboratoire de Planétologie et Géodynamique de Nantes (LPGN), UMR-CNRS 6112,
Université de Nantes.

2 rue de la Houssinière, 44322 Nantes Cedex (FRANCE)

phone: +33 (0) 2 5112 5491

fax: +33 (0) 2 5112 5268

*E-mail: yann.morizet@univ-nantes.fr

Abstract

Silica undersaturated melts such as nephelinites are very peculiar magmatic materials. Their occurrence on Earth is often associated with carbonatite melts. These low-silica melts can dissolve a large quantity of CO₂ and are rich in alkalis. However, the way CO₂ dissolves into these melts and the effect of different alkali elements are poorly constrained.

We present experimental results on the CO₂ solubility and speciation in synthetic nephelinite in the NKCMA system, equilibrated at high-pressure (50-300 MPa), high-temperature (1250°C) with an excess C-O-H fluid phase. The nephelinitic glasses with 20 mol.% total alkali oxides were synthesized with varying K₂O/(K₂O+Na₂O) ratio (denoted as #K) in order to investigate the differential effect of those two alkali cations on CO₂ solubility and speciation. All experiments were conducted under oxidizing conditions (>NNO+3) resulting in binary fluid phase compositions with CO₂ and H₂O species. The CO₂ content and speciation were investigated using Micro-Raman and Solid State NMR spectroscopies for ¹³C nucleus.

We observe an increase in CO₂ content as a function of pressure, consistent with previous studies but CO₂ solubility is much higher than in alkali-poorer melts. The CO₂ content is above 1 wt.% at 50 MPa and increases up to 4.5 wt.% at 300 MPa. The progressive replacement of Na by K (#K between 0 and 1) induces an increase in CO₂ content. At 50 MPa, the CO₂ solubility is ~1.75 wt.% in the K-free glass (#K = 0) and increases up to ~3.0 wt.% CO₂ in Na-free glass (#K = 1). The change in CO₂ solubility as a function of #K is discussed in terms of carbonatite genesis.

The ¹³C NMR spectra show that carbonate (CO₃²⁻) environments can be attributed to carbonate species associated to non-bridging oxygen in agreement with the depolymerized nature of the investigated compositions. Two singular additional carbonated species were also

identified with ^{13}C NMR signatures at 161 and 165 ppm. Those species are assigned to isolated $\text{K}^+ \dots \text{CO}_3^{2-} \dots \text{H}^+$ and $\text{Na}^+ \dots \text{CO}_3^{2-} \dots \text{H}^+$ carbonate species. The presence of such isolated carbonate species is interpreted as possible precursors to carbonatitic melt genesis.

1. Introduction

A large range of fluid compositions are present in the deep Earth and these have an important influence on various Earth processes (e.g. Eggler, 1974; Brey and Green, 1975, 1976; Wallace and Green, 1988; Falloon and Green, 1989; Hirose, 1997; Freda et al., 1997; Draper and Green, 1997; Dalton and Presnall, 1998). Carbon dioxide (CO₂) is the second most abundant magmatic volatile (e.g. Gerlach and Graeber, 1985; Symonds et al., 1994; Jambon, 1994) being even dominant in some volcanic systems (Roedder, 1965; Wyllie and Huang, 1976; Holloway, 1981; Giggenbach, 1997; Andersen and Neumann, 2001). Some of these systems may reflect a high CO₂ abundance in their source regions, as witnessed by unusual magma compositions (such as nephelinite, melilitite and kamafugite) which have been suggested to result from high CO₂ activity during mantle melting (e.g. Holloway, 1976; Wallace and Green, 1988; Johnson et al., 1994; Dixon and Stolper, 1995b; Papale and Polacci, 1999; De Moor et al., 2013). Recent experimental investigations have also argued that CO₂-rich source could play a major role on the genesis of ocean island basalts and associated alkali-rich magmas (Dasgupta et al., 2007; Gerbode and Dasgupta, 2010; Mallik and Dasgupta, 2013).

The genesis of those alkali-rich magmatic compositions is often associated to CO₂ incorporation, which might trigger the increase in alkali content in the silicate melts (Iacono-Marziano et al., 2008; Mitchell, 2009). Alkali-rich and CO₂-rich silicate magmas are indeed commonly associated to carbonatite rocks. For instance, several recent studies have shown the co-existence of CO₂-rich (several wt.% CO₂) nephelinite silicate melts (40-50 wt.% SiO₂ and >20 wt.% Na₂O+K₂O) with carbonatite melts in natural melt inclusions collected at Oldoinyo Lengai volcano (Mitchell, 2009; Mitchell and Dawson, 2012; De Moor et al., 2013)

The role of intensive parameters (T,P) on either CO₂ or H₂O solubilities and speciations in silicate melts are well constrained (e.g. Blank and Brooker, 1994; Dixon et al., 1995a; Morizet et al., 2002, 2010; Behrens et al., 2009; Lesne et al., 2011a,b). The effect of melt composition is also reasonably well understood, and available studies cover various types of compositions ranging from basalts and affiliates (e.g. Fine and Stolper, 1986; Pan et al., 1991; Pawley et al., 1992; Dixon et al., 1995a; Botcharnikov et al., 2005, 2006; Iacono-Marziano et al., 2008; Shishkina et al., 2010; Lesne et al., 2011a,b) to rhyolites (e.g. Fogel and Rutherford, 1990; Blank et al., 1993; Tamic et al., 2001; Duncan and Dasgupta, 2014) and silica undersaturated melts (e.g. Brey and Green, 1976; Thibault and Holloway, 1994; Brooker et al., 2001a; Behrens et al., 2009). As a result, several thermodynamic and/or empirical models with the scope of predicting the CO₂ solubility as function of compositional and intensive parameters have been proposed (Dixon, 1997; Papale, 1999; Brooker et al., 2001a; Newman and Lowenstern, 2002; Papale et al., 2006; Lesne et al., 2011b, Iacono-Marziano et al., 2012). Furthermore, recent work by Guillot and Sator (2011) based on classical molecular dynamic simulations reproduces adequately the CO₂ solubility and physical properties of CO₂-bearing basaltic and kimberlitic melts at pressures up to 12 GPa. However, although CO₂ dissolution mechanisms have been specifically studied (e.g. Fine and Stolper, 1986; Fogel and Rutherford, 1990; Blank and Brooker, 1994), the structure of CO₂-bearing silicate melts is still poorly known. In particular, there is currently a lack of knowledge on the role of network modifying and charge balancing cations such as Na or K.

The intermixing between alkali and/or alkaline-earth in silicate melts is recognized to exert a non-negligible influence on the silicate melt structure and physical properties. Recent work by Le Losq and Neuville (2013) on rhyolitic polymerized melt composition identified a strong effect of K/Na ratio on the silicate melt structural and physical properties in CO₂-free melt composition; hence, as CO₂ is dependent on the melt structural configuration, an effect

of K/Na ratio on CO₂ solubility and speciation is to be expected. In their work, Le Losq and Neuville (2013) showed that with increasing K/Na ratio, there is an increase in rhyolitic melt viscosity which they attributed to geometrical changes within the melt structure as K is progressively replaced by Na (i.e. changes in Si-O bond length and Si-O-Si bond angles). However, in Le Losq and Neuville (2013), the intermixing between Na and K in the studied rhyolitic composition does not induce a change in the degree of polymerization.

The degree of silicate melt polymerization is commonly expressed as the NBO/T ratio (Mysen, 1988; 1990) where NBO represents the concentration of Non-Bridging Oxygen associated with the presence non-network-forming or network modifier cations (Na⁺, K⁺, Ca²⁺ and Mg²⁺ in the present study) and T is the concentration of network forming cations (Si⁴⁺ and Al³⁺ in the present study). In other words, according to Le Losq and Neuville (2013), the intermixing between Na and K cations in silicate melt involves local structural rearrangements without changing the NBO/T which is kept constant.

Early work by Brooker et al. (2001a) showed that the NBO/T influences dramatically the CO₂ solubility in silicate glasses: an increase in the NBO/T provokes an increase in CO₂ solubility. Therefore, in the present study, several issues of varying importance have to be considered when investigating the systematic of CO₂ solubility in silicate melts. Brooker et al. (2001a) identified the change in CO₂ solubility with varying NBO/T which can be considered as a first order effect. The differential effect of K versus Na on CO₂ solubility in silicate melt could be considered as a second order effect; yet it is currently poorly known. Consequently, in the case a change in CO₂ solubility is observed with changing K/Na ratio in the presented work, it would reflect a difference in the chemical affinity of CO₂ with either Na or K cations rather than a change in the NBO/T.

We investigated the effect of the exchange between K and Na on the CO₂ solubility and speciation of a nephelinitic glass composition. We conducted our experimental study at 1250°C and between 50 and 300 MPa on five different starting compositions with #K (molar K₂O/(K₂O+Na₂O) ratio) ranging from 0 to 1. The CO₂ solubility and speciation in glass were investigated via Raman and NMR spectroscopies.

2. Experimental synthesis

A synthetic Fe-free nephelinitic starting composition was prepared from a mixture of dried oxides (²⁸SiO₂, ²⁹SiO₂, Al₂O₃, CaO and MgO) and carbonates (Na₂¹³CO₃ and K₂¹³CO₃). The absence of iron is justified by the analytical needs for investigating the C speciation with NMR which cannot be used on Fe-rich materials. The investigated nephelinitic composition is similar to the one reported in Brooker et al. (2001a) with (in mol.%) SiO₂ = 45, Al₂O₃ = 7, MgO = 13, CaO = 15, and Na₂O+K₂O = 20. The investigated composition is also very close to natural occurrences of nephelinitic silicate melt compositions found in melt inclusions from Oldoinyo Lengai volcano (Mitchell and Dawson, 2012; De Moor et al., 2013). As a comparison, the theoretical compositions are given in Table 1 along with some examples of the silicate melt compositions found in melt inclusions by Mitchell and Dawson (2012) and De Moor et al. (2013). As shown in Table 1, the investigated synthetic compositions are close to the reported natural compositions in melt inclusions: 1) the Na₂O+K₂O in mol.% is on the same order in both synthetic compositions (20 mol.%) and natural melt inclusions (20 to 26 mol.%); 2) the investigated degree of polymerization in the synthetic compositions is intermediate (NBO/T = 1.4) as compared to the natural ones for which the NBO/T is ranging from 0.74 to 2.08. The CaO and MgO contents are different in between natural and synthetic

compositions owing to the fact that Fe is not present in our synthetic compositions for the NMR analytical purpose.

In order to investigate the role of alkali exchange on the CO₂ solubility and speciation, Na and K were substituted for each other on a molar basis producing five different starting materials with different #K ranging from 0 to 1 (Table 1): K0-E, 20 mol.% Na₂O, 0 mol.% K₂O (#K = 0); K5-E, 15 mol.% Na₂O, 5 mol.% K₂O (#K = 0.25); K10-E, 10 mol.% Na₂O, 10 mol.% K₂O (#K = 0.5); K15-E, 5 mol.% Na₂O, 15 mol.% K₂O (#K = 0.75); and K20-E, 0 mol.% Na₂O, 20 mol.% K₂O (#K = 1). Although, natural nephelinitic melt inclusions exhibit #K close to the sodic end-member (Table 1, #K < 0.3), we cover #K between 0 and 1 so as to obtain a systematic view of the CO₂ content variation as a function of alkali composition. A small proportion of Fe₂O₃ (< 0.4 wt.%) was added as a source of paramagnetic element to reduce the NMR acquisition time length by reducing the relaxation time which is usually long for ¹³C (Kohn et al., 1991). The FeO^{tot} was quantified by EPMA and is reported in Table 2. The measured FeO^{tot} in the starting materials is below 0.3 mol.% which is known not to affect NMR spectra (Maekawa et al., 1991). The compositions from EPMA for the whole set of samples are reported in Table 2.

The carbonate powders (Na₂¹³CO₃ and/or K₂¹³CO₃) are the source of ¹³CO₂ during the experiments. The total CO₂ content is broadly similar between the different starting compositions: 13.2 wt.% ¹³CO₂ for K0, K5, K15 and K20-E and 14.62 wt.% ¹³CO₂ for K10-E. Up to 6 wt.% H₂O is added together as liquid water with the solid starting materials in the platinum capsules (see Table 2). As shown in Table 2, the loaded water content is different from one experiment to another but remains almost constant from one sample to another at a given pressure. The starting composition is loaded after water and the platinum capsule is welded shut.

Experiments were conducted at 1250°C in an Internally Heated Pressure Vessel (IHPV) for run durations between 2 to 5 hours which is sufficient to ensure bulk chemical equilibrium considering that at 1250°C CO₂ and H₂O diffusion coefficients are high (Watson, 1994; Zhang et al., 2007). Pressure varied between 50 and 300 MPa (Table 2). An additional set of samples was synthesised at 100 MPa under CO₂-free conditions (K-E5 denoted 100 MPa CO₂-free) but in equilibrium with water (see Table 2). For technical reasons, the experiment could not be conducted at 1250°C but instead at 1150°C. We believe that such difference will not produce any significant difference for the purpose of the present study. This experimental pressure range ($50 < P < 300$ MPa) is close to the reported entrapment pressure in natural melt inclusions studied by De Moor et al. (2013). As for the temperature, De Moor et al. (2013) did not specify a range of equilibrated temperature but suggested that the melt inclusions at some point experienced high enough temperature preventing immiscibility between silicate and carbonate liquids (Brooker and Kjarsgaard, 2011).

The procedure to achieve the experimental conditions is described elsewhere (e.g., Scaillet et al., 1992) and is summarized as follows. The IHPV is first loaded at room temperature with Argon gas to roughly half the desired total pressure value. The temperature is then brought to the final value and the pressure increases up to requested experimental pressure. P and T are constantly monitored during the experiment using an electronic gauge for P and a type S thermocouple connected to a Eurotherm controller for T. The T gradient along the capsule (2 cm in length) was measured with an additional S-type thermocouple and never exceeded 15°C. Reported P, T measurements are accurate to within ± 20 bars and $\pm 5^\circ\text{C}$, respectively.

All runs were ended by drop-quenching the sample holder into the cold part of the IHPV, which resulted in quench rates of 150°C/s for that kind of apparatus (Di Carlo et al., 2006; Iacono-Marziano et al., 2008; Morizet et al., 2010). In all cases, opening of the capsules

produced a hissing sound suggesting that an excess fluid phase was present in the capsule during the experiment. Several chips from the recovered glasses were selected for micro-Raman analyses. The remaining of the glass sample was then crushed for MAS NMR analysis. Optical examination of the recovered samples was done. Unfortunately, we could not find any fluid inclusions preventing the fluid phase composition to be determined by analytical mean. All the investigated samples are clear glasses. Samples showing evidence of crystals (for instance K20-E, K15-E synthesized at 200 and 300 MPa; K10-E synthesized at 300 MPa) were discarded. The K10-E2 sample synthesized at 200 MPa showed evidence of a crystalline phase; we nevertheless considered this sample as it is still informative within the frame of the current work. All recovered synthesized samples are listed in Table 2.

3. Analytical techniques

3.1 Confocal Micro-Raman

Confocal micro-Raman was used to characterize the volatile species dissolved in the glass samples. The Raman system is a Jobin-Yvon Labram spectrometer (focal distance = 300 mm) equipped with a 2400 gratings/mm CCD detector. The light source is an Ar laser Innova 300-5W from Coherent© operating at 514.5 nm. The typical output laser power was set between 100 and 150 mW. The analyses were performed in confocal mode (hole = 500 μm , slit = 200 μm) with an Olympus (x50) objective. The spectra were recorded to characterize the network and CO_3^{2-} vibrational modes in the 200-1200 cm^{-1} range and the OH stretching band in the 2500-3900 cm^{-1} range. The spectral frequency position was measured with the emission lines of Ne- and Hg-lamps. The accuracy stays within $\pm 1 \text{ cm}^{-1}$. The acquisition time was usually within 45-90 s to obtain a reasonably good signal to noise ratio (S/N). Two to five Raman

spectra were collected on several spot locations to check for sample homogeneity with regards to its dissolved volatile contents (H₂O and CO₂).

3.2 ¹³C-MAS NMR

Solid State ¹³C-MAS NMR analyses of the partially crushed samples were performed with a 500 MHz Bruker Avance III. A 4 mm CP/MAS probe was employed and the samples loaded in a ZrO₂ rotor with Teflon end-cap. Rotors were spun at 10 kHz. All spectra are referenced against TMS (Tetramethylsilane).

For all samples, ¹³C-MAS NMR spectra were acquired with single $\pi/4$ excitation of 2 μ s. ¹³C-species can have long spin lattice relaxation time in silicate glasses (several minutes, Kohn et al., 1991). As a result, a recycle delay between scans of at least 20 s was used. ¹H decoupling during acquisition (SPINAL64 scheme with a rf field of 60 kHz, Fung et al., 2000) was used to prevent from broadening of the ¹³C lines due to heteronuclear interactions with protons (Laws et al., 2002). For ¹³C Direct MAS spectra, up to 2560 scans have been co-added. The obtained free-induction-decay signal was treated with a low line broadening exponential function (50 Hz) preventing from loss of structural information.

{¹H}-¹³C CPMAS NMR sequence was also employed to investigate ¹H and ¹³C proximity and spatial relationship in the glass (Schmidt et al., 2000; Robert et al., 2001; Puls and Eckert, 2006). This method is selective but non quantitative. We applied a contact time (ct) length of 1 ms. During CP-MAS experiment, a ¹H repetition time of 1 s was sufficient for total relaxation before the next scan. The 2D heteronuclear correlation spectrum (¹H-¹³C HETCOR) for K0-E1 was acquired similarly except for the contact time set to 2 ms.

^1H - ^1H EXCHANGE NMR acquisition was also conducted so as to investigate the inter-atomic proximity between proton environments in K0-E1 glass. In this experiment, rotor was spun at 14 kHz. A number of 2048 scans were collected at a recycle delay of 1 s. We used a mixing time of 1 and 500 ms. At 1 ms mixing time, the exchange between the proton is reduced and most of the hydroxyl signal will be located on the diagonal of the 2D NMR spectrum whereas at 500 ms mixing time the exchange between the proton is enhanced and the hydroxyl signal will start to depart from the 2D NMR spectrum diagonal.

3.3 EPMA

The major element compositions of glasses were measured using EPMA. Measurements were done on a Cameca SX 50, with 15kV and 10 nA, with 10 s peak counting time for all elements. Na and K were analysed first and a PAP correction procedure was applied. Na migration under the beam was corrected by using secondary hydrous glass standards of known Na_2O and H_2O contents (Clemente et al., 2004). Analyses were conducted in defocused mode (10 μm beam diameter) in order to reduce any elemental loss. Measurements have been conducted to evaluate the alkali loss under the electron beam. The Na/K is almost constant in analysed glasses: for example after 15 s of analysing time, the loss in Na as compared to K in K5-E1 is less than 5% in relative on the counting value. The average major elements concentrations (in mol.%) obtained from more than 20 analyses for each recovered glasses are reported in Table 2. The standard deviation for each oxide is below 0.3 mol.%.

4. Methods and Results

4.1 CO_2 content determined via micro-Raman spectroscopy

The glass CO₂ content was determined from micro-Raman spectroscopy using the calibration method of Morizet et al. (2013). We show a typical example of the adopted procedure in Figure 1 for identical experimental pressure (117 MPa) except for K5-E2 which was synthesized at 200 MPa. To obtain an idea of the statistical distribution of the silicate glass species (Rossano and Mysen, 2013), we have first considered the volatile-free glasses (VF). Starting from the reliable simulation of the VF spectra, we have followed the same approach for CO₂-bearing glasses. We added an additional peak at 1070 cm⁻¹ to simulate the CO₃²⁻ vibrational signature (see Figure 1). The whole set of peak parameters (peak position, full width at half maximum FWHM and areas) were then optimized until obtaining the lowest possible residuals as shown in Figure 1. The CO₂ dissolved in the glass was then calculated from the proposed linear equation in Morizet et al. (2013) which is independent of the glass composition. The reader is referred to this article for further information on the method.

The corresponding CO₃/Qⁿ HF ratio needed for the CO₂ estimate is reported in Table 2, along with the corresponding wt.% CO₂. The CO₃/Qⁿ HF given value represents the average value determined from the replicated Raman analyses on the different spot locations. We observe a clear increase in the ν₁ CO₃ peak with increasing synthesis pressure when comparing the spectra for K0-E3 (Figure 1A) and K5-E2 (Figure 1B). The increase in peak intensity is witnessing an increase in CO₂ solubility with increasing pressure, as anticipated (e.g. Blank and Brooker, 1994; Thibault and Holloway, 1994; Brooker et al., 1999; Morizet et al., 2002; Botcharnikov et al., 2005, 2006; Behrens et al., 2009).

If we compare the spectra obtained for samples synthesized under identical experimental pressure (K0-E3, K10-E3 and K15-E3 in Figure 1A, C and D, respectively), we observe that the resulting CO₃/Qⁿ is increasing from 0.149 for K0-E3 to 0.186 for K15-E3. This increase is well above the standard deviation calculated from replicated Raman spectra, and outside the error associated with the simulation procedure (error of ±0.018 on the CO₃/HF reported in

Morizet et al., 2013); therefore such an increase may be attributed to an actual change in the CO₂ solubility with composition. Overall, the very low errors indicate the good homogeneity of the recovered glass samples.

The H₂O dissolved in the glass was determined from micro-Raman spectroscopy using the calibration procedure of Mercier et al. (2009). The presence of the CO₂ peak in the high-frequency (HF: 800-1200 cm⁻¹) region of the Raman spectra prevents the use of this frequency region to determine the H₂O content (see Mercier et al., 2009); therefore, we determined the glass H₂O solubility (H₂O^{tot}) using the low-frequency (LF: 250-800 cm⁻¹) region. For mafic magmas, there is a linear correlation between this ratio and the glass water content (see Mercier et al., 2009; and Table 2). Typical Raman spectra are shown in Figure 2 with the LF region for carbonates (Figure 2A and C) and the HF region of water species (Figure 2B and D). Below each spectrum the third-order polynomial fitted baseline for quantifying the area of the different frequency region is also shown (i.e. LF and H₂O). The ratio between the H₂O and the LF bands is reported next to each spectrum.

We show the spectra for K0 glass samples synthesized at different pressure. The H₂O/LF ratio varies between samples suggesting a different H₂O content. For instance, we see a change in H₂O/LF ratio between 0.455 and 0.538 between K0-E3 and K0-E2, respectively; for K0-E1, the H₂O/LF goes down to 0.420. We note that the standard deviation (based on replicate Raman spectra) on the H₂O/LF ratios can be high, hinting at a slight heterogeneity of the H₂O solubility of the glass samples. However, the difference in the H₂O/LF primarily reflects a difference in H₂O solubility which in large part comes from the different amounts of H₂O loaded to experimental charges (see Table 2), in addition to possible effects of K₂O on H₂O solubility (see below). The H₂O content in K-E5 glass samples (100 MPa CO₂-free) is very close to the initial H₂O content loaded in the capsule suggesting a fairly good accuracy of the Mercier et al. (2009) method in determining the H₂O content in the present

glass compositions. As an example, 2.92 wt.% H₂O was measured in K0-E5 for an initial H₂O content of 3.25 wt.% (see Table 2). The close agreement between the loaded and measured H₂O content also indicates that the experimental charges were not saturated with respect to water and the measured H₂O content does not represent the actual H₂O solubility.

4.2 Carbonate speciation from ¹³C MAS NMR spectroscopy

The CO₂ speciation has been investigated by ¹³C MAS NMR. We show in Figure 3 several ¹³C MAS NMR spectra obtained with various acquisition methods: single pulse or CPMAS. The spectra are represented at a given pressure (Figure 3A, B and C at 300, 200 and 100 MPa, respectively) and for a given glass composition (Figure 3D, E and F for K0, K5 and K10, respectively). Below the spectra we have also added the difference between two selected NMR spectra. We have reported the ¹³C NMR spectra between 155 and 185 ppm for the carbonate region. We did not find evidence for the presence of CO₂^{mol} at 125 ppm (Kohn et al., 1991; Morizet et al., 2002) suggesting that CO₂ is dissolved only as carbonate groups (CO₃²⁻) in the investigated composition in agreement with the results of Brooker et al. (2001b) on a similar composition.

The CO₃²⁻ NMR signature is represented by a main peak located between 165 and 175 ppm. The line shape of this main CO₃²⁻ contribution is slightly asymmetric. The asymmetry is consistent with the existence of several CO₃²⁻ groups within the glass structure (Kohn et al., 1991; Brooker et al., 1999; Morizet et al., 2002; 2010). The existence of several CO₃²⁻ environments is also confirmed by the complex changes in the difference spectra (Figure 3D, E and F). For instance, in Figure 3E, we observe a diminution of the spectra difference as compared to the average line around 168 ppm whereas we observe a growth in the spectra difference as compared to the average line at 171 ppm. A similar observation can be made for

K0 (Figure 3D) and K10 (Figure 3F), though the K10 sample synthesized at 200 MPa is partially crystallized. Comparing the spectra at a given pressure also gives evidence for several carbonate units dissolved in glasses of different compositions. The most important change is observed in Figure 3C for samples synthesized at 100 MPa. The spectra difference between K15 and K0 shows a strong diminution at 170 ppm whereas we observe a noticeable growth at 168 ppm. It is difficult to find any systematic change as a function of synthesis pressure or glass composition; only relevant spectrum simulations will provide quantitative information.

The main CO_3^{2-} band is accompanied by additional signatures. In Figure 3C, we see two weak peaks located at 164.7 and 161.7 ppm, respectively. Those peaks are also visible in other plots from Figure 3. The assignment of these two peaks is unambiguous and has been well-documented at least for crystalline material: the 164.7 ppm peak is attributed to free hydrated sodium carbonate group (Nebel et al., 2008) and the 161.7 ppm peak is attributed to free hydrated potassium carbonate group (Gasc et al., 2009). These two distinct species are present in the glass as free clusters. The peaks indicating the presence of those free clusters are observed in samples free of crystalline material (clear glass) and are therefore considered to be part of the glass. In Figure 3D, E and F, we also added a $\{^1\text{H}\}\text{-}^{13}\text{C}$ CPMAS NMR spectrum for K0, K5 and K10 synthesized under different pressures. It appears that the peaks for the hydrated (Na,K) ... CO_3 increase compared to the main carbonate peak under CPMAS acquisition.

5. Discussion

5.1 CO_2 and H_2O solubilities: the effect of composition

We show in Figure 4 the change in CO₂ and H₂O contents, determined by Raman spectroscopy, as a function of the #K as determined from EPMA analyses (numerical values are given in Table 2). In Figure 4A, we clearly see an increase in CO₂ content with increasing #K. The H₂O content is reported next to each point in Figure 4A. At 300 MPa, the CO₂ content changes from 3.7 to 4.4 wt.% CO₂ between K0 and K5 (i.e. #K = 0 and 0.251, respectively). The same applies to 200 MPa data point with an increase of CO₂ content from 3.1 to 3.6 wt.% CO₂ for K0 and K5, respectively. We also show an additional point (K10-E2) showing a slight increase in CO₂ content as compared to K5-E2, noting that this sample has a non-negligible amount of crystalline material. SEM elemental mapping revealed that most of the crystalline phase is composed of sodium. At 100 and 50 MPa, we still observe the increase in CO₂ content with increasing K₂O content; however, there seems to be a plateau in CO₂ content for #K between 0.5 and 0.75 (K10 and K15, respectively). At 50 MPa, this plateau is followed by a strong increase in CO₂ content for K20-E4.

The measured CO₂ content range for the investigated compositions and at the given intensive conditions ($50 < P < 300$ MPa) is the highest one measured so far in silicate melt. Thibault and Holloway (1994) measured a similar range for CO₂ solubility in Ca-leucitite but at higher pressure: between 3 and 4 wt.% CO₂ at 1.0 GPa. The Ca-leucitite composition studied by Thibault and Holloway (1994) has an NBO/T = 0.99 very close to our studied compositions (NBO/T ~ 1.4); Ca-leucitite composition is alkali-poor (Na₂O+K₂O = 6.65 wt.%) as compared to our compositions (Na₂O+K₂O > 20 wt.%). Owing to the change in chemical composition in between the mentioned compositions, the total alkali concentration is a strong control on the CO₂ solubility as inferred by recent thermodynamic modelling (Iacono-Marziano et al., 2012) as compared to the total alkaline earth concentration.

The increase in CO₂ solubility with increasing K₂O content is also accompanied by an increase in H₂O solubility. We show in Figure 4B the change in the H₂O glass content with

increasing #K. For all investigated pressures, we observe a slight increase in H₂O content with increasing #K in glass. This increase in H₂O content with increasing #K in glass is also observed at almost constant water activity in the fluid phase (see Table 2 for X H₂O fluid). At 200 MPa, the H₂O content changes from 1.4 to 1.8 wt.% H₂O between K0-E2 and K10-E2. At 100 MPa, the change in H₂O solubility is on the same order between 1.2 and 1.6 wt.% H₂O between K0-E3 and K15-E3.

The change in CO₂ and H₂O solubilities might be correlated. Recent work by Behrens et al. (2009), Lesne et al. (2011a,b), and Iacono-Marziano et al. (2012) suggest that H₂O dissolution in silicate melt enhances that of CO₂. Therefore, it is possible that the increase in CO₂ is due to the effect of H₂O and not to the increase in K₂O content. This potential increase in CO₂ solubility with increasing H₂O content might be related to the water dissolution mechanism which is known to induce a depolymerization of the aluminosilicate melt structure (Kuemmerlen et al., 1992; Zotov and Keppler, 1998; Robert et al., 2001), therefore providing available NBOs for CO₂ molecules to dissolve as CO₃²⁻ group. Whereas this mechanism applies adequately to polymerized aluminosilicate compositions (NBO/T close to 0), it does not straightforwardly applies for depolymerized aluminosilicate compositions. Xue and Kanzaki, (2004) showed that H₂O dissolution in depolymerized silicate composition does not induce an additional depolymerization and could on the contrary induce a polymerization. Furthermore, for a similar composition (foidite from Behrens et al., 2009), Iacono-Marziano et al. (2012) quantified the increase in CO₂ solubility with increasing H₂O content. They found that changing the H₂O content between 2.0 and 3.0 wt.% H₂O does not appreciably change CO₂ solubility. Hence, we propose that the increasing K₂O content induces an increase in both CO₂ and H₂O solubilities.

Figure 5A displays the change in volatile content (CO₂ and H₂O) for the whole set of glasses synthesized at different pressures and for all #K compositions (except for K-E5 synthesised at

100 MPa and CO₂-free). Clearly, there is a gradual increase in both H₂O and CO₂ contents (at fixed #K); while the opposite is generally observed in common silicate melt compositions (i.e. dissolved CO₂ and H₂O are inversely correlated). The co-increase in H₂O and CO₂ appears to follow one linear trend except for samples synthesized at 300 MPa which plot at CO₂ contents slightly higher relative to the main trend. We have indicated next to each data point, the measured #K. As shown in Figure 4 and inferred from Figure 5, we see that the highest CO₂ and H₂O contents are always observed for the higher #K values.

In an attempt to disentangle the relative roles of either $a_{\text{H}_2\text{O}}$ or #K on CO₂ solubility, we have calculated the CO₂ activity, here expressed as the ratio between the wt.% CO₂ and the CO₂ fugacity ($X_{\text{CO}_2}^{\text{fl}} \times f^{\text{fl}}\text{CO}_2$) in the system. The fugacity of pure CO₂ ($f^{\text{fl}}\text{CO}_2$) is calculated using the CORK equation of Holland and Powell (1991). The results are shown as a function of #K (Figure 5B) and H₂O content (Figure 5C). Considering the entire data set, a broad positive correlation is apparent, which suggests that exchanging K for Na altogether increases CO₂ solubility. In detail, however, at each specific pressure, the increase is highly nonlinear: in the #K range 0-0.5 a gentle increase of the wt.% CO₂/ $f^{\text{fl}}\text{CO}_2$ ratio with increasing K₂O content is observed; from #K 0.5 to 0.75, this ratio dampens, even decreasing somewhat, to eventually increase again beyond #K = 0.75. In contrast, no obvious correlation between the wt.% CO₂/ $f^{\text{fl}}\text{CO}_2$ ratio and dissolved H₂O can be extracted from Figure 5C which suggests that the behaviour observed in Figure 5B is due to the change in $X_{\text{K}_2\text{O}}$ and not to the change in $a_{\text{H}_2\text{O}}$. Furthermore, we observe a clear effect of pressure onto the wt.% CO₂/ $f^{\text{fl}}\text{CO}_2$. For instance, comparing the low pressure experiments at 50 MPa (K-E4) and high pressure experiments at 300 MPa (K-E1), we observe that the wt.% CO₂/ $f^{\text{fl}}\text{CO}_2$ ratio strongly increases between 300 and 50 MPa. It suggests that the solution mechanism for CO₂ molecules is enhanced at low pressure as compared to higher pressure. It also implies that the activity of CO₂ is less ideal at high pressure.

Results shown in Figure 4 and 5 suggest that the exchange of Na by K induces an important increase in CO₂ solubility and a more modest increase in H₂O solubility. Recent work by Scaillet and Pichavant (2005) suggested that the increase in melt K₂O content was a main factor controlling the CO₂ solubility, and Papale et al. (2006) and Iacono-Marziano et al., (2012) modeling also concluded to a possible effect of the network modifying cation (alkali and alkaline earth) on the CO₂ solubility. Yet the differential effect of Na and K on CO₂ solubility was not clearly assessed. The model derived by Dixon (1997) tried to address the differential effect of melt cations on the CO₂ solubility based on the Π parameter. In the Π parameter, the effect of K⁺ on CO₂ solubility is more important than the effect of Na⁺. Our results presented in Figure 4 confirm this point; however, the anticipated change in CO₂ solubility with the addition of K⁺ instead of Na⁺ from the Π parameter is less than our results show. Although, the Π parameter model from Dixon (1997) is not calibrated for a wide range of composition (i.e. alkali content below 12.0 wt.% in Dixon (1997)), we calculated the Π parameter for our compositions. Between #K = 0 and 1, the calculated Π parameter changes from 3.5 to 3.9 in agreement with the increase in CO₂ solubility with increasing K₂O content.

We also calculated the change in CO₂ solubility in our glass compositions using the model of Papale et al. (2006). We performed the calculations with two different fluid phase compositions: 1) X CO₂^{fl} = 1, X H₂O^{fl} = 0 and 2) X CO₂^{fl} = 0.65, X H₂O^{fl} = 0.35. The former case is very close to the suspected fluid phase compositions in our experiments (see Table 2). Both sets of calculations were carried out at 300 MPa and 1250°C. For X CO₂^{fl} = 1, the calculation results are consistent with the observed trend in CO₂ solubility with increasing K₂O content. Although the CO₂ solubility values calculated are different from our experimental results; between #K = 0 and 1, Papale et al. (2006) thermodynamic model suggest an increase in CO₂ solubility between 0.92 and 2.03. In other words, the CO₂ solubility would be doubled between K0 and K20 glass compositions. However, calculations

performed with $X_{\text{CO}_2}^{\text{fl}} = 0.65$ leads to almost no change in CO_2 solubility in between K0 and K20: 0.17 wt.% CO_2 for $\#K = 0$ and 0.19 wt.% CO_2 for $\#K = 1$. In a certain way, our CO_2 solubility experimental results are in agreement with both Dixon (1997) and Papale et al. (2006) models; however, additional parametrization might be useful.

At 50 MPa, the CO_2 solubility increases twice between 5 and 20 mol.% K_2O (15 and 0 mol.% Na_2O). This finding readily explains the close association documented worldwide between K-rich magmatism and enhanced CO_2 activity, as summarised in the introduction. It follows that K-rich magmas might be potentially CO_2 -rich reservoirs in the upper crust, as compared to the more sodic varieties. Similarly, the generation of K-rich mantle melts will be a potent and efficient CO_2 -sink mechanism of any CO_2 reservoir stored in the deep Earth. Finally, our results highlight once again (see also Lesne et al., 2011a,b) that barometric estimates based on dissolved volatile contents of glass inclusions trapped in phenocrysts may be seriously in error (for instance overestimated trapping pressure).

5.2 Carbonate speciation as a function of #K

^{13}C MAS NMR spectra shown in Figure 3 witness a complex environment for CO_3^{2-} molecules in the glass. Moreover, the spectra differences reported in Figure 3 indicate that the CO_3^{2-} global spectral signature is a complex convolution of several individual carbonate environments. Considering that we observe two clear features from the difference spectrum (see Figure 3) underneath the main CO_3^{2-} contribution, we suspect that at least two individual CO_3^{2-} environments are present. To assess such an hypothesis, we performed a simulation of the ^{13}C MAS NMR spectra using statistical distribution with several Gaussian peaks; however, we did not obtain a reasonable interpretable solution explaining the complex

change in carbonate speciation as observed in Figure 3. The subtle differences observed in Figure 3 cannot be resolved with our actual NMR data.

In Figure 6, we provide a comparison between ^{13}C MAS spectra obtained for different CO_2 -bearing glass compositions: haplo-phonolite (NCMAS system) synthesised at 2.0 GPa and 1350°C obtained from Morizet et al. (2002); diopside ($\text{CaMgSi}_2\text{O}_6$) synthesised at 1.0 GPa and 1580°C obtained from Morizet (2002). We compare the ^{13}C MAS NMR spectra with two of our ^{13}C MAS NMR spectra (K0-E3 and K15-E3). The whole set of glass compositions shows different degree of polymerization: haplo-phonolite glass is slightly depolymerized with $\text{NBO}/\text{T} = 0.2$ whereas diopside glass is strongly depolymerized with $\text{NBO}/\text{T} = 2$ and the investigated alkali-rich nephelinitic glass has an $\text{NBO}/\text{T} \sim 1.39$.

We represent also the spectrum simulation following the work of Morizet et al. (2002) using four Gaussian peaks. Morizet et al. (2002) identified a peak at 168.4 ppm and attributed it to NBO-carb. $\text{M}^{\text{n+}}$, where a CO_3^{2-} molecule is connected to a NBO and charge compensated by a surrounding cation ($\text{M}^{\text{n+}}$). This CO_3^{2-} configuration in depolymerized compositions has been inferred from previous spectroscopic studies (Blank and Brooker, 1994; Brooker et al., 2001b; Morizet et al., 2010). The other Gaussian peaks were attributed to network carbonates consistent with the high degree of polymerization of the haplo-phonolite glass. Diopside glass exhibits a ^{13}C peak centered at 167.6 ppm. Our investigated glasses have a ^{13}C ppm shift at higher value around 169-170 ppm. This comparison suggests that CO_2 in the nephelinitic glasses is dissolved as NBO-carb. $\text{M}^{\text{n+}}$ only; the ^{13}C MAS NMR peak does not extend towards the identified region for network carbonates (see Figure 6).

Considering the high alkali concentrations in our investigated compositions (see Table 1), it is likely that the charge compensating cation is either Na^+ or K^+ or both Na^+ and K^+ . It might also be possible for Ca^{2+} and Mg^{2+} to be part of this charge compensating role; however, in

the highly depolymerized diopside glass ^{13}C NMR spectrum, the peak is centered at lower ppm shift (167.6 ppm) as compared to the one observed for K0-E3 and K15-E3. This also suggests that the nature of the charge compensating cation induces a shift in the ^{13}C MAS NMR peak. If this difference seems clear between alkali (K0 and K15) and alkaline-earth (diopside), it appears difficult to constrain any change in ^{13}C chemical shift between K-free (K0-E3) and K-bearing (K15-E3). Early investigation for crystalline carbonates by Papenguth et al. (1989) showed that the difference in ^{13}C chemical shift is limited. For instance, Li_2CO_3 and Na_2CO_3 exhibit a ^{13}C chemical shift at 168.4 and 169.8 ppm, respectively. This difference can be resolved for crystalline carbonates showing sharp NMR signature but cannot be adequately resolved for amorphous CO_2 -bearing glasses.

5.3 Free carbonate clusters as precursors to liquid immiscibility: Carbonatite liquid genesis

The existence of free hydrated carbonate groups ($(\text{K}^+, \text{Na}^+) \dots \text{CO}_3^{2-} \dots \text{H}$; see Figure 3) is intriguing. Such free units are likely to constitute precursors to immiscible carbonatite liquids. Brooker et al. (2001b) proposed that free carbonate groups dissolved in melt are observed in alkali-rich melts; our results are in agreement with such a statement. The existence of isolated hydrated carbonate groups also implies that at some stage an oxygen atom is consumed as a result of the CO_2 molecules dissolution. Such isolated units might have a strong ionic character as suggested in previous studies (Genge et al., 1995; Williams and Knittle, 2003; Morizet et al., 2013), and potentially a high electrical conductivity as well (Gaillard et al., 2008).

We have shown in Figure 3, that the isolated carbonate units are hydrated in character (see CPMAS NMR spectra in Figure 3). $\{^1\text{H}\}$ - ^{13}C HETCOR NMR spectra for K0-E1 was

conducted so as to better constrain the hydration of these particular species. The spectrum is reported in Figure 7A. We observe that the main CO_3^{2-} signature (169.8 ppm assigned to the main carbonates species) is associated with hydrogen atoms with a ^1H NMR shift centered at 5.0 ppm. The ^1H NMR shift in silicate glasses has been extensively studied (e.g. Eckert et al., 1988; Kummerlen et al., 1992; Riemer et al., 2000; Schmidt et al., 2000; Cody et al., 2005; Xue and Kanzaki, 2008). The ^1H ppm shift centered at 5.0 ppm can be attributed to hydrogen atoms with different configurations: SiOH, water molecules in the vicinity of SiO_4 tetrahedra.

We observe from Figure 7A that the isolated $\text{Na}^+ \dots \text{CO}_3^{2-} \dots \text{H}^+$ (~ 165 ^{13}C ppm shift) are associated to a particular ^1H signature (~ 14 ppm ^1H ppm shift). NMR investigations of proton environments have shown that the position of the ^1H NMR shift is correlated to the distance between the hydrogen and oxygen atoms and can be considered as a witness of the hydrogen bond strength (Yesinowski and Eckert, 1987; Eckert et al., 1988; Xue and Kanzaki, 2007): the higher the ^1H ppm shift, the shorter hydrogen – oxygen atoms distance. In Figure 7, the $\text{Na}^+ \dots \text{CO}_3^{2-} \dots \text{H}^+$ unit is related to hydrogen atoms with a very short distance from the oxygen atom. This observation confirms the fact that such a unit occurs as an isolated cluster. It is also in agreement with the fact that hydrogen atoms or water is probably a key parameter for the formation of carbonate melt (Genge et al., 1995; Williams and Knittle, 2003).

We also show additional ^1H - ^1H EXCHANGE NMR experiment in Figure 7B and C acquired with two different mixing time (1 and 500 ms). In the 1 ms spectrum (Figure 7B), the distribution of the proton environments is located along the diagonal and the two main proton contributions seen in the $\{^1\text{H}\}$ - ^{13}C HETCOR NMR are not distinguished. Under this mixing time, the spin diffusion is not efficient and an individual proton will see an individual proton of the same nature (i.e. same molecular environment). In the 500 ms spectrum (Figure 7C), we observe two distinct proton correlations: one is associated to a proton environment at +5.0 ppm and one is associated to the proton environment at +14 ppm. The former at +5.0 ppm

exhibits a strong NMR signature extending broadly off the diagonal. This shows that all the hydroxyl environments are correlated to each other due to strong spin diffusion. The latter narrow signature at +14 ppm on the contrary is remaining exclusively on the diagonal confirming that this proton environment attributed to $\text{Na}^+ \dots \text{CO}_3^{2-} \dots \text{H}^+$ is isolated from the hydroxyl environments in the glass.

Recent review by Jones et al. (2013) summarized the atomic properties of carbonate melts. The carbonate melts exhibit a unique property different from silicate melts: ionic character with a trigonal symmetry CO_3^{2-} molecule compensated by a metal cation. In the present study, we show that the metal cation involved in the carbonatitic precursor is probably an alkali. Recent work by Mitchell (2009) on immiscibility textures from Oldoinyo Lengai melt inclusions suggests that the carbonate immiscible liquid phase is alkali-rich as compared to alkaline-earth cation.

Whether the genesis of such melt is favoured by the presence of Na or K can also be discussed in term of CO_2 solubility difference between Na-rich and K-rich melts. We have shown that CO_2 solubility in nephelinitic melt is increased by K relative to Na. Hence, K-rich silicate melts can accommodate more CO_2 in their structure than those Na-rich; therefore the lower CO_2 solubility level of Na-rich silicate melt makes them good candidates to produce an exsolved carbonate melt precursor to natrocarbonatite natural melts. Furthermore, the suspected increase of network carbonate units in K-rich melt will prevent an efficient immiscibility K-rich carbonatitic melt. Although, we do not have currently natural examples of K-rich (in comparison with Na) carbonatitic melt (Jones et al., 2013), recent experimental work (Thomsen and Schmidt, 2008; Grassi and Schmidt, 2011; Tsuno et al., 2012) witnessed the potential existence of K-rich (relative to Na) carbonatite liquid obtained from the partial melting of carbonated natural pelites.

6. Concluding remarks

In the present experimental study conducted at high pressures (50 – 300 MPa) and high temperature (1250°C), we have shown that a silica undersaturated melt (nephelinite) can dissolve several wt.% CO₂. The determined CO₂ solubility appears to be several orders of magnitude higher than the CO₂ solubility measured in silicate melts so far, at comparable P-T conditions. Our objective was to investigate the possible change in CO₂ solubility with different alkali cations. We have shown that the exchange between Na and K induces a significant change in CO₂ solubility. Increasing the K₂O molar fraction (i.e. decreasing the Na₂O molar fraction) in the bulk composition causes an increase in the CO₂ solubility suggesting that potassium-rich melts can accommodate more CO₂ molecules in their structure than those are sodium-rich. This result is only preliminary, and more work is necessary to fully investigate the systematic changes in CO₂ solubility as a function of other compositional variables (e.g. Ca/(Ca+Mg), Fe³⁺/(Fe²⁺+Fe³⁺)).

The CO₂ speciation study reveals the presence of several CO₃²⁻ environments, possibly connected to non-bridging oxygens but also in network configuration in the melt. An additional NMR signature was found which can be attributed to isolated carbonate environments. The existence of such isolated units has major implications for the petrogenesis of carbonatite as they can constitute the precursors of carbonatitic melts.

Acknowledgements

The authors are grateful to the ANR agency which financed the current through the ANR-2010-BLAN-621 “Electrolith”. The authors thank the University of Orléans, the University

of Nantes and the CNRS for their access to analytical facilities. We also much appreciated the constructive reviews by two anonymous reviewers which greatly improved the quality of the manuscript. Rajdeep Dasgupta is thanked for handling our manuscript and for his detailed comments.

References

Andersen T. and Neumann E. -R. (2001) Fluid inclusions in mantle xenoliths. *Lithos* **55**, 301-320.

Behrens H., Misiti V., Freda C., Vetere F., Botcharnikov R. E. and Scarlato P. (2009) Solubility of H₂O and CO₂ in ultrapotassic melts at 1200 and 1250°C and pressure from 50 to 500 MPa. *Am. Mineral.* **94**, 105-120.

Blank J. G. and Brooker R. A. (1994) Experimental studies of carbon dioxide in silicate melts: solubility, speciation and stable carbon isotope behaviour. In *Volatiles in magmas Reviews in Mineralogy* (eds. M. R. Carroll, J. R. Holloway). Mineral. Soc. Am., Washington, DC, **30**, pp 157-186.

Blank J. G., Stolper E. M. and Carroll M. R. (1993) Solubilities of carbon dioxide and water in rhyolitic melt at 850°C and 750 bars. *Earth Planet. Sci. Lett.* **119**, 27-36.

Botcharnikov R. E., Freise M., Holtz F., and Behrens H. (2005) Solubility of C-O-H mixtures in natural melts: new experimental data and application range of recent models. *Ann. Geophys.* **48**, 634-646.

Botcharnikov R. E., Behrens H. and Holtz F. (2006) Solubility and speciation of C-O-H fluids in andesitic melt at T=1100-1300°C and P=200 and 500 MPa. *Chem. Geol.* **229**, 125-143.

Brey G. P. and Green D. H. (1975) The role of CO₂ in the genesis of olivine melilitites. *Contrib. Miner. Petrol.* **49**, 93-103.

Brey G. P. and Green D. H. (1976) Solubility of CO₂ in Olivine Melilitite at high pressures and role of CO₂ in the Earth's Upper mantle. *Contrib. Miner. Petrol.* **55**, 217-230.

Brooker R. A. and Kjarsgaard B. A. (2011) Silicate-Carbonate liquid immiscibility and phase relations in the system SiO₂-Na₂O-Al₂O₃-CaO-CO₂ at 0.1-0.25 GPa with applications to carbonatite genesis. *J. Petrol.* **52**, 1281-1305.

Brooker R. A., Kohn S. C., Holloway J. R., McMillan P. F. and Carroll M. R. (1999) Solubility, speciation and dissolution mechanisms for CO₂ in melts on the NaAlO₂-SiO₂ join. *Geochim. Cosmochim. Acta* **63**, 3549-3565.

Brooker R. A., Kohn S. C., Holloway J. R., and McMillan P. F. (2001a) Structural controls on the solubility of CO₂ in silicate melts. Part I: Bulk solubility data. *Chem. Geol.* **174**, 225-240.

Brooker R. A., Kohn S. C., Holloway J. R. and McMillan P. F. (2001b) Structural controls on the solubility of CO₂ in silicate melts. Part II: IR characteristics of carbonate groups in silicate glasses. *Chem. Geol.* **174**, 241-254.

Clemente B., Scaillet B. and Pichavant M. (2004) The solubility of sulphur in hydrous rhyolitic melts. *J. Petrol.* **45(11)**, 2171-2196.

Cody G. D., Mysen B. O. and Lee S. K. (2005) Structure vs. composition: A solid-state ¹H and ²⁹Si NMR study of quenched glasses along the Na₂O-SiO₂-H₂O join. *Geochim. Cosmochim. Acta* **69(9)**, 2373-2384.

Dalton J. A. and Presnall D. C. (1998) The Continuum of Primary Carbonatitic-Kimberlitic Melt Compositions in Equilibrium with Lherzolite: Data from the System CaO-MgO-Al₂O₃-SiO₂-CO₂ at 6 GPa. *J. Petrol.* **39**, 1953-1964.

Dasgupta R., Hirschmann M. M. and Smith N. D. (2007) Partial melting experiments of peridotite + CO₂ at 3 GPa and genesis of alkalic ocean island basalts. *J. Petrol.* **48**, 2093-2124.

De Moor J. M., Fischer T. P., King P. L., Botcharnikov R. E., Hervig R. L., Hilton D. R., Barry P. H., Mangasini F. and Ramirez C. (2013) Volatile-rich silicate melts from Oldoinyo Lengai volcano (Tanzania): Implications for carbonatite genesis and eruptive behavior. *Earth Planet. Sci. Lett.* **361**, 379-390.

Di Carlo I., Pichavant M., Rotolo S. G. and Scaillet B. (2006) Experimental crystallization of a high-K arc basalt: The golden pumice, Stromboli volcano (Italy). *J. Petrol.* **47**, 1317-1343.

Dixon J. E. (1997) Degassing of alkalic basalts. *Am. Mineral.* **82**, 368-378.

Dixon J. E. and Stolper E. M. (1995b) An experimental study of water and carbon dioxide solubilities in Mid-Ocean Ridge Basaltic liquids. Part II: Applications to degassing. *J. Petrol.* **36**, 1633-1646.

Dixon J. E., Stolper E. M. and Holloway J. R. (1995a) An experimental study of water and carbon dioxide solubilities in Mid-Ocean Ridge Basaltic liquids. Part I: Calibration and solubility models. *J. Petrol.* **36**, 1607-1631.

Draper D. S. and Green D. H. (1997) P-T phase relations of silicic alkaline, aluminous mantle xenolith glasses under anhydrous and C-O-H fluid saturated conditions. *J. Petrol.* **38**, 1187-1224.

Duncan M. S. and Dasgupta R. (2014) CO₂ solubility and speciation in rhyolitic sediment partial melts at 1.5-3.0 GPa – Implications for carbon flux in subduction zones. *Geochim. Cosmochim. Acta* **124**, 328-347.

Eckert H., Yesinowski J. P., Silver L. A. and Stolper E. M. (1988) Water in silicate glasses: Quantification and structural studies by ¹H Solid Echo and MAS-NMR methods. *J. Phys. Chem.* **92**, 2055-2064.

Eggler D. H. (1974) Effect of CO₂ on the melting of peridotite. *Carnegie Institute Washington Yearbook* **73**, 215-224.

Falloon T. J. and Green D. H. (1989) The solidus of carbonated, fertile peridotite. *Earth Planet. Sci. Lett.* **94**, 364-370.

Fine G. and Stolper E. M. (1986) Dissolved carbon dioxide in basaltic glasses: concentrations and speciation. *Earth Planet. Sci. Lett.* **76**, 263-278.

Fogel R. A. and Rutherford M. J. (1990) The solubility of carbon dioxide in rhyolitic melts: A quantitative FTIR study. *Am. Mineral.* **75**, 1311-1326.

Freda C., Gaeta M., Palladino D. M. and Trigila R. (1997) The Villa Senni Eruption (Alban Hills, Central Italy): The role of H₂O and CO₂ on the magma chamber evolution and on the eruptive scenario. *J. Volc. Geoth. Res.* **78**, 103-120.

Fung B. M., Khitritin A. K. and Ermolaev K. (2000) An improved broadband decoupling sequence for liquid crystals and solids. *J. Magn. Reson.* **142**, 97-101.

Gaillard F., Malki M., Iacono-Marziano G., Pichavant M. and Scaillet B. (2008) Carbonatite melts and electrical conductivity in the asthenosphere. *Science* **322**, 1363-1365.

Gasc F., Thiebaud-Roux S. and Mouloungui Z. (2009) Methods for synthesizing diethyl carbonate from ethanol and supercritical carbon dioxide by one-pot or two-step reactions in the presence of potassium carbonate. *J. Supercrit. Fluids* **50**, 46-53.

Genge M. J., Jones A. P. and Price G. D. (1995) An infrared and Raman study of carbonate glasses: Implications for the structure of carbonatite magmas. *Geochim. Cosmochim. Acta* **59**, 927-937.

Gerbode C. and Dasgupta R. (2010) Carbonate-fluxed melting of MORB-like pyroxenite at 2.9 GPa and genesis of HIMU Ocean Island Basalts. *J. Petrol.* **51**, 2067-2088.

Gerlach T. M. and Graeber E. J. (1985) Volatile budget of Kilauea volcano. *Nature* **313**, 273-277.

Giggenbach W. F. (1997) Relative importance of thermodynamic and kinetic processes in governing the chemical and isotopic composition of carbon gases in high-heat flow sedimentary basins. *Geochim. Cosmochim. Acta* **61**, 3763-3785.

Grassi D. and Schmidt M.W. (2011) The melting of carbonated pelites from 70 to 700 km depth. *J. Petrol.* **52**, 765-789.

Hirose K. (1997) Partial melt compositions of carbonated peridotite at 3 GPa and role of CO₂ in alkali-basalt magma generation. *Geophys. Res. Lett.* **24**, 2837-2840.

Holloway J. R. (1976) Fluids in the evolution of granitic magmas: Consequences of finite CO₂ solubility. *Geol. Soc. Am. Bull.* **87**, 1513-1518.

Holloway J. R. (1981) Volatile interactions in magmas. In *Thermodynamics of Melts and Minerals (Advances in Physical Geochemistry I)* (eds. R. C. Newton, A. Navrotsky and B.J Wood) Springer-Verlag, New York, pp 273-293.

Iacono-Marziano G., Gaillard F. and Pichavant M. (2008) Limestone assimilation by basaltic magmas: an experimental re-assessment and application to Italian volcanoes. *Contrib. Miner. Petrol.* **155**, 719-738.

Iacono-Marziano G., Morizet Y., Le Trong E. and Gaillard F. (2012) New experimental data and semi-empirical parameterization of H₂O-CO₂ solubility in mafic melts. *Geochim. Cosmochim. Acta* **97**, 1-23.

Jambon A. (1994) Earth degassing and large-scale geochemical cycling of volatile elements. In: *Volatiles in magmas. (Reviews in mineralogy)*. (eds. M. R. Carroll, J. R. Holloway) Mineral. Soc. Am., Washington, DC, **30**, pp 479-517.

Johnson, M.C., Anderson, A.T., and Rutherford, M.J. (1994) The pre-eruptive volatile contents of magmas. In: *Volatiles in magmas. (Reviews in mineralogy)*. (eds. M. R. Carroll, J. R. Holloway) Mineral. Soc. Am., Washington, DC, **30**, pp 280-329.

Jones A. P., Genge M. and Carmody L. (2013) Carbonate melts and carbonatites. In *Carbon in Earth. Review in mineralogy and Geochemistry*. (eds. R. M. Hazen, A. P. Jones and J. A. Baross) Mineral. Soc. Am., Washington, DC, **75**, pp 289-322.

Kohn S. C., Brooker R. A. and Dupree R. (1991) ^{13}C MAS NMR: A method for studying CO_2 speciation in glasses. *Geochim. Cosmochim. Acta* **55**, 3879-3884.

Kuemmerlen J., Merwin L. H., Sebald A. and Keppler H. (1992) Structural role of H_2O in sodium silicate glasses: results from ^{29}Si and ^1H NMR spectroscopy. *J. Phys. Chem.* **96**, 6405-6410.

Laws D. D., Bitter H. M. L. and Jerschow A. (2002) Solid-state NMR spectroscopic methods in chemistry. *Angew. Chem. Int. Ed.* **41**, 3096-3129.

Le Losq C. and Neuville D. R. (2013) Effect of the Na/K mixing on the structure and the rheology of tectosilicate silica-rich melts. *Chem. Geol.* **346**, 57-71.

Lesne P., Scaillet B., Pichavant M., Iacono-Marziano G. and Beny J. M. (2011a). The H_2O solubility of alkali basaltic melts: an experimental study. *Contrib. Miner. Petrol.* **162**, 133-151. DOI: 10.1007/s00410-010-0588-x.

Lesne P., Scaillet B., Pichavant M. and Beny J. M. (2011b) The carbon dioxide solubility in alkali basalts: an experimental study. *Contrib. Miner. Petrol.* **162**, 153-168. DOI: 10.1007/s00410-010-0585-0.

Maekawa H., Maekawa T., Kawamura K. and Yokokawa, T. (1991) The structural groups of alkali silicate glasses determined from ^{29}Si MAS NMR. *J. Non-Cryst. Solids* **127**, 53-64.

Mallik A. and Dasgupta R. (2013) Reactive infiltration of MORB-eclogite-derived carbonated silicate melt into fertile peridotite at 3 GPa and genesis of alkalic magmas. *J Petrol.* **54**, 2267-2300.

Mercier M., Di Muro A., Giordano D., Métrich N., Lesne P., Pichavant M., Scaillet B. and Clocchiatti R. (2009) Influence of glass polymerisation and oxidation on micro-Raman water analysis in alumino-silicate glasses. *Geochim. Cosmochim. Acta* **73**, 197-217.

Mitchell R. H. (2009) Peralkaline nephelinite-natrocarbonatite immiscibility and carbonatite assimilation at Oldoinyo Lengai, Tanzania. *Contrib. Miner. Petrol.* **158**, 589-598.

Mitchell R. H. and Dawson J. B. (2012) Carbonate-silicate immiscibility and extremely peralkaline silicate glasses from Nasira cone and recent eruptions at Oldoinyo Lengai volcano, Tanzania. *Lithos* **152**, 40-46.

Morizet Y., Kohn S. C. and Brooker R. A. (2001) Annealing experiments on CO₂-bearing jadeite glass: an insight into the true temperature dependence of CO₂ speciation in silicate melts. *Min. Mag.* **65**, 701-707.

Morizet Y. (2002) Carbon dioxide in magmatic systems; experimental studies of CO₂ solubility and speciation. Ph. D. thesis, University of Bristol.

Morizet Y., Brooker R. A. and Kohn S. C. (2002) CO₂ in haplo-phonolite Melt: Solubility, speciation and carbonate complexation. *Geochim. Cosmochim. Acta* **66**, 1809-1820.

Morizet Y., Paris M., Gaillard F. and Scaillet B. (2010) C-O-H fluid solubility in haplobasalt under reducing conditions: An experimental study. *Chem. Geol.* **279**, 1-16.

Morizet Y., Brooker R. A., Iacono-Marziano G. and Kjarsgaard B. (2013) Quantification of CO₂ dissolved in silicate glasses of various compositions with Micro-Raman spectroscopy. *Am. Mineral.* **98**, 1788-1802.

Mysen B. O. (1988) Structure and properties of silicate melts. *Developments in Geochemistry*, vol. 4. Elsevier, Amsterdam, 354 pp.

Mysen B. O. (1990) Effect of pressure, temperature, and bulk composition on the structure and species distribution in depolymerized alkali aluminosilicate melts and quenched melts. *J. Geophys. Res. B* **95**, 15733-15744.

Nebel H. N. M., Mayer C. and Epple M. (2008) On the structure of amorphous calcium carbonate - A detailed study by solid-state NMR spectroscopy. *Inorg. Chem.* **47**, 7874-7879.

Newman S. and Lowenstern J. B. (2002) VOLATILECALC: a silicate melt-H₂O-CO₂ solution model written in Visual Basic for excel, Source. *Comput. Geosci.* **28**, 597-604.

Pan V., Holloway J. R. and Hervig R. (1991) The pressure and temperature dependence of carbon dioxide solubility in tholeiitic basalt melts. *Geochim. Cosmochim. Acta* **55**, 1587-1595.

Papale P. (1999) Modeling of the solubility of a two-component H₂O + CO₂ fluid in silicate liquids. *Am. Mineral.* **84**, 477-492.

Papale P. and Polacci M. (1999) Role of carbon dioxide in the dynamics of magma ascent in explosive eruptions. *Bull. Volc.* **60**, 583-594.

Papale P., Moretti R. and Barbato D. (2006) The compositional dependence of the saturation surface of H₂O+CO₂ fluids in silicate melts. *Chem. Geol.* **229**, 78-95.

Papenguth H. W., Kirkpatrick R. J., Montez B. and Sandberg P. A. (1989) ¹³C MAS NMR spectroscopy of inorganic and biogenic carbonates. *Am. Mineral.* **74**, 1152-1158.

Pawley A. R., Holloway J. R. and McMillan P. F. (1992) The effect of oxygen fugacity on the solubility of carbon-oxygen fluids in basaltic melt. *Earth Planet. Sci. Lett.* **110**, 213-225.

Puls S. P. and Eckert H. (2006) Site discrimination in mixed-alkali glasses studied by Cross-Polarization NMR. *J. Phys. Chem. B* **110**, 14253-14261.

Riemer T., Schmidt B., Behrens H. and Dupree R. (2000) H₂O/OH ratio determination in hydrous aluminosilicate glasses by static proton NMR and the effect of chemical shift anisotropy. *Solid State Nucl. Magn. Reson.* **15**, 201-207.

Robert E., Whittington A., Fayon F., Pichavant M. and Massiot D. (2001) Structural characterization of water-bearing silicate and aluminosilicate glasses by high-resolution solid-state NMR. *Chem. Geol.* **174**, 291-305.

Roedder E. (1965) Liquid CO₂ inclusions in olivine bearing nodules and phenocrysts from basalts. *Am. Mineral.* **50**, 1746-1782.

Rossano S. and Mysen B. O. (2013) Raman spectroscopy of silicate glasses and melts in geological system. In *Raman spectroscopy applied to Earth Sciences and Cultural Heritage (EMU notes in Mineralogy)* (eds. J. Dubessy, M. C. Caumon, F. Rull) Mineralogical Society of America, **12**, pp 321-366.

Scaillet B. and Pichavant M. (2005) A model of sulphur solubility for hydrous mafic melts: application to the determination of magmatic fluid compositions of Italian volcanoes. *Ann. Geophys.* **48(4/5)**, 671-697.

Scaillet B., Pichavant M., Roux J., Humbert G. and Lefèvre A. (1992) Improvements of the Shaw membrane technique for measurement and control of fH₂ at high temperatures and pressures. *Am. Mineral.* **77**, 647-655.

Schmidt B. C., Riemer T., Kohn S. C., Behrens H. and Dupree R. (2000) Different water solubility mechanisms in hydrous glasses along the Qz-Ab Join: Evidence from NMR Spectroscopy. *Geochim. Cosmochim. Acta* **64**, 513-526.

Shishkina T. A., Botcharnikov R. E., Holtz F., Almeev R. R. and Portnyagin M. V. (2010) Solubility of H₂O- and CO₂-bearing fluids in tholeiitic basalts at pressures up to 500 MPa. *Chem. Geol.* **277**, 115-125.

Symonds R. B., Rose W. I., Bluth G. J. S. and Gerlach T. M. (1994) Volcanic-gas studies: Methods, Results and Applications. In *Volatiles in magmas. (Review in mineralogy)*. (eds. M. R. Carroll, J. R. Holloway) Mineral. Soc. Am., Washington, DC, **30**, pp 1-66.

Tamic N., Behrens H. and Holtz F. (2001) The solubility of H₂O and CO₂ in rhyolitic melts in equilibrium with a mixed CO₂-H₂O fluid phase. *Chem. Geol.* **174**, 333-347.

Thibault Y. and Holloway J. R. (1994) Solubility of CO₂ in a Ca-rich leucitite: Effects of pressure, temperature and oxygen fugacity. *Contrib. Miner. Petrol.* **116**, 216-224.

Thomsen T. B. and Schmidt M. W. (2008) Melting of carbonated pelites at 2.5-5.0 GPa, silicate-carbonatite liquid immiscibility, and potassium-carbon metasomatism of the mantle. *Earth Planet. Sci. Lett.* **267**, 17-31.

Tsuno K., Dasgupta R., Danielson L. and Richter K. (2012) Flux of carbonate melt from deeply subducted pelitic sediments - geophysical and geochemical implications for the source of Central American volcanic arc. *Geophys. Res. Lett.* **39**, L16307, doi:10.1029/2012GL052606.

Wallace M. E. and Green D. H. (1988) An experimental determination of primary carbonatite magma composition. *Nature* **335**, 343-346.

Watson E. B. (1994) Diffusion in volatile-bearing magmas. In *Volatiles in Magmas. (Reviews in Mineralogy)*. (eds. M. R. Carroll, J. R. Holloway) Mineral. Soc. Am., Washington, DC **30**, pp 370-411.

Williams Q. and Knittle E. (2003) Structural complexity in carbonatite liquid at high pressures. *Geophys. Res. Lett.* **30**, doi:10.1029/2001GL013876.

Wyllie P. J. and Huang W. -L. (1976) Carbonation and melting in the system CaO-MgO-SiO₂-CO₂ at mantle pressures with geophysical and petrological applications. *Contrib. Miner. Petrol.* **54**, 79-107.

- Xue X. and Kanzaki M. (2004) Dissolution mechanisms of water in depolymerised silicate melts: constraints from ^1H and ^{29}Si NMR spectroscopy and ab initio calculations. *Geochim. Cosmochim. Acta* **68**, 5027-5057.
- Xue X. and Kanzaki M. (2007) High-Pressure $\delta\text{-Al}(\text{OH})_3$ and $\delta\text{-AlOOH}$ Phases and Isostructural Hydroxides/Oxyhydroxides: New Structural Insights from High-Resolution ^1H and ^{27}Al NMR. *J. Phys. Chem. B* **111**, 13156-13166.
- Xue X. and Kanzaki M. (2008) Structure of hydrous aluminosilicate glasses along the diopside-anorthite join: A comprehensive one- and two-dimensional ^1H and ^{27}Al NMR study. *Geochim. Cosmochim. Acta* **72**, 2331-2348.
- Yesinowski J. P. and Eckert H. (1987) Hydrogen environments in calcium phosphates: proton MAS NMR at high spinning speeds. *J. Am. Chem. Soc.* **109**, 6274-6282.
- Zhang Y., Xu Z., Mengfan Z. and Wang H. (2007) Silicate melt properties and volcanic eruptions. *Rev. Geophys.* **45**, 216-242.
- Zotov N. and Keppler H. (1998) The influence of water on the structure of hydrous sodium tetrasilicate glasses. *Am. Mineral.* **83**, 823-834.

Figure caption

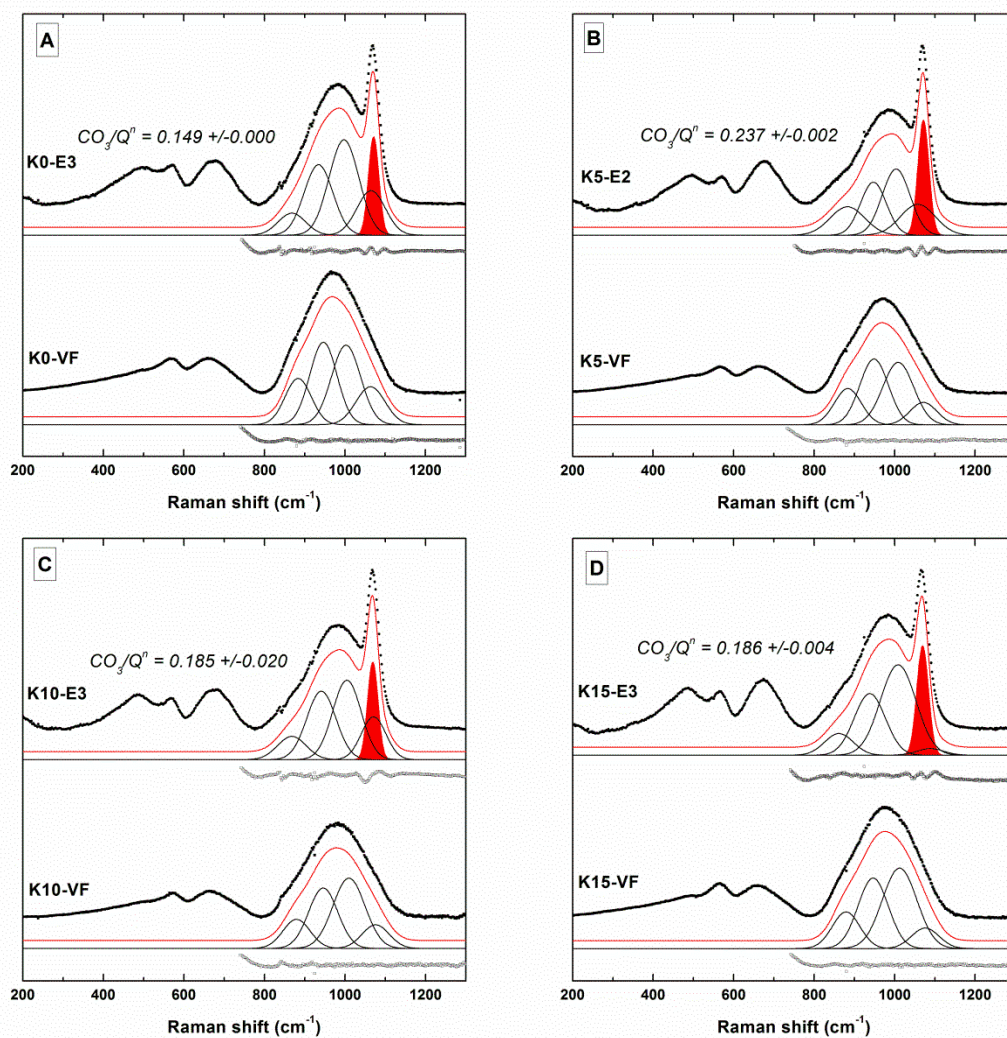


Figure 1

Figure 1. Typical Raman spectra obtained for different nephelinitic glass samples: A, K0; B, K5; C, K10; D, K15. Spectra obtained on CO₂-bearing and volatile-free (VF) are reported. The CO₂ content was determined using the calibration method from Morizet et al.

(2013). The high-frequency envelope (800-1200 cm^{-1}) was first simulated for VF spectra considering four individual Gaussian peaks. For CO_2 -bearing, the spectrum simulation was conducted by adding an additional peak for $\nu_1 \text{CO}_3$ peak vibrational signature at $\sim 1080 \text{ cm}^{-1}$. The CO_3/Q^n ratio obtained from the simulation is reported next to each spectrum and the residual from the simulation is shown underneath the spectra.

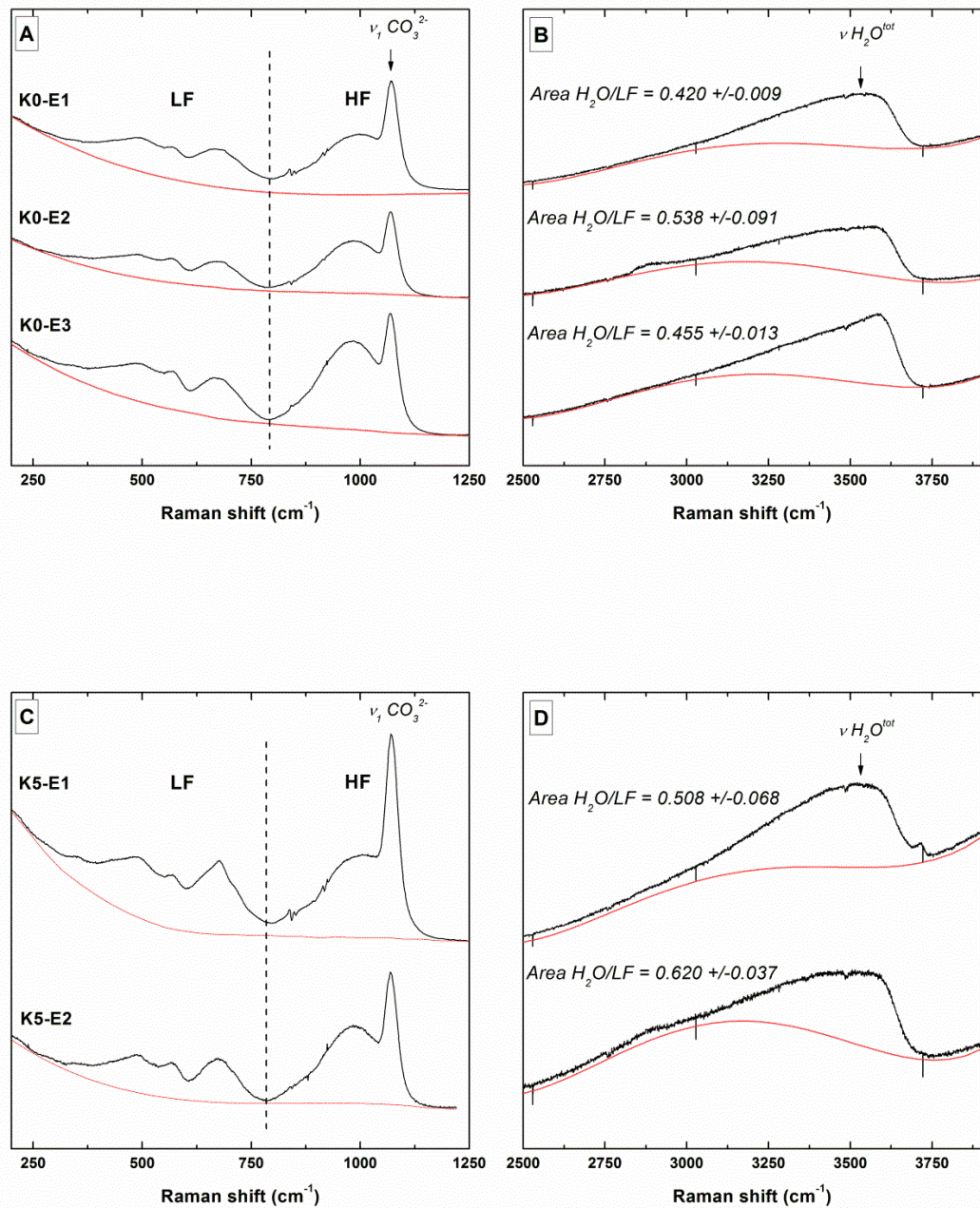


Figure 2. Typical Raman spectra obtained for H₂O quantification in glasses. The spectra are presented for two typical glass compositions: K0 (A) and K5 (C); and shown for the silicate glass frequency region (LF 200-800 cm⁻¹ and HF 800-1200 cm⁻¹ in A and C) and the H₂O frequency region (2500-3900 cm⁻¹ in B and D). A typical third-order polynomial baseline curve is reported underneath each Raman spectrum. The H₂O content was determined with the calibration method established by Mercier et al. (2009) and using the areas ratio between H₂O and the LF regions (shown next to each spectrum).

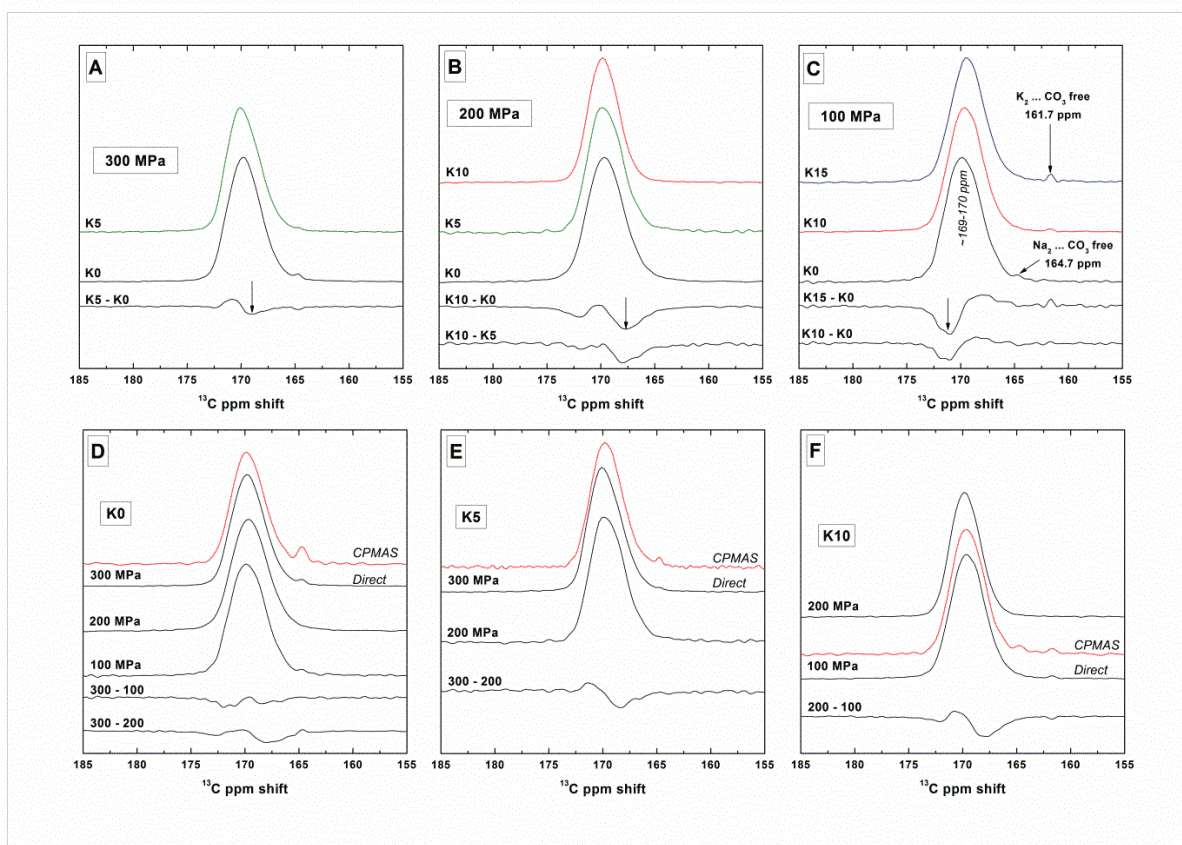


Figure 3. ¹³C MAS NMR spectra obtained for glass samples 1) synthesized at different pressure: 300 (A), 200 (B) and 100 MPa (C); 2) of different composition: K0 (D), K5 (E) and K10 (F). Spectra were acquired under Direct (single pulse) or {¹H}-¹³C CPMAS NMR conditions. The difference between two spectra is also shown underneath the spectra in

each plot. The arrows shown in plots A to C are informative and show the possible existence of individual carbonate component.

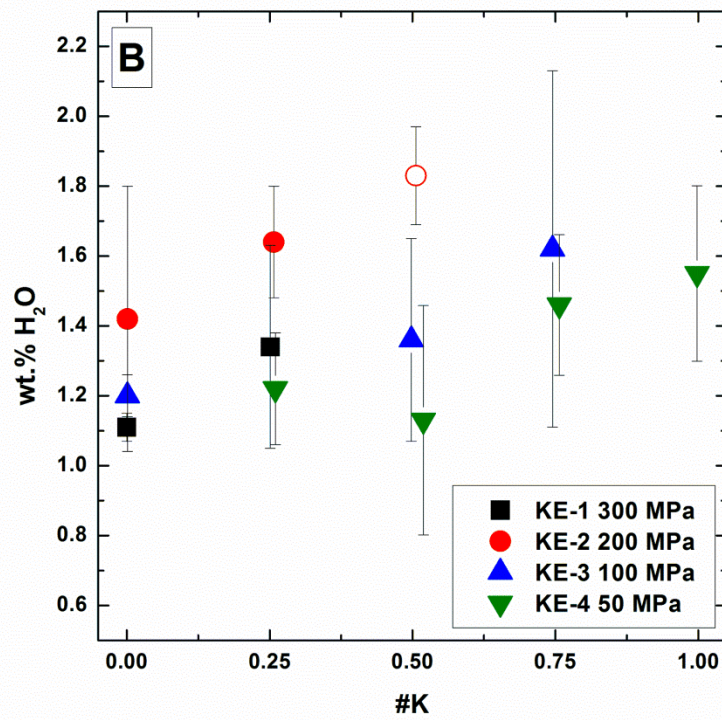
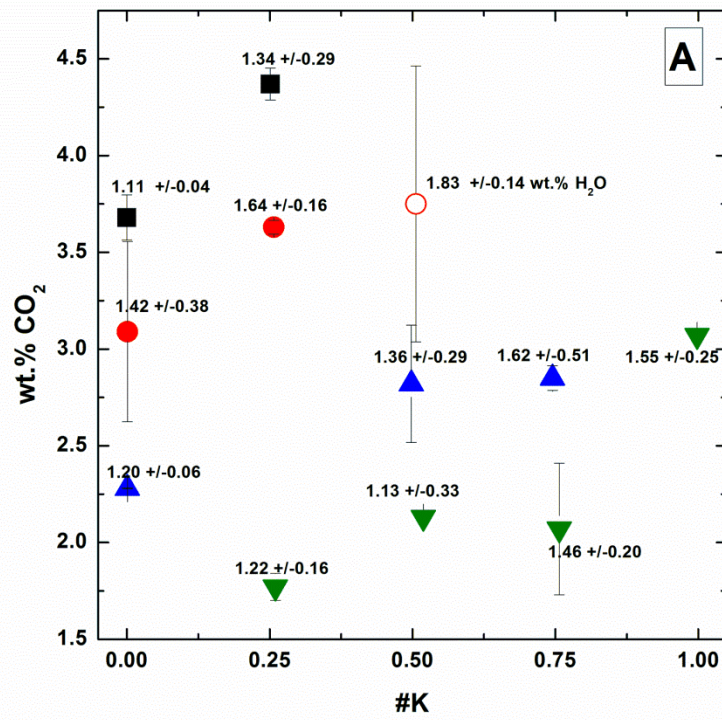


Figure 4. Change in CO₂ (A) and H₂O (B) solubilities in glasses as a function of #K (see Table 1 and 2). In (A), we indicate the determined H₂O content for each glass sample from Raman. The error bars reported for each corresponds to the standard deviation from replicated Raman analyses; therefore representing the homogeneity/heterogeneity of the CO₂ and H₂O contents in each glass sample. The open symbol corresponds to the CO₂ and H₂O contents determined for glass sample showing evidences of crystalline material (K10-E2 in Table 2).

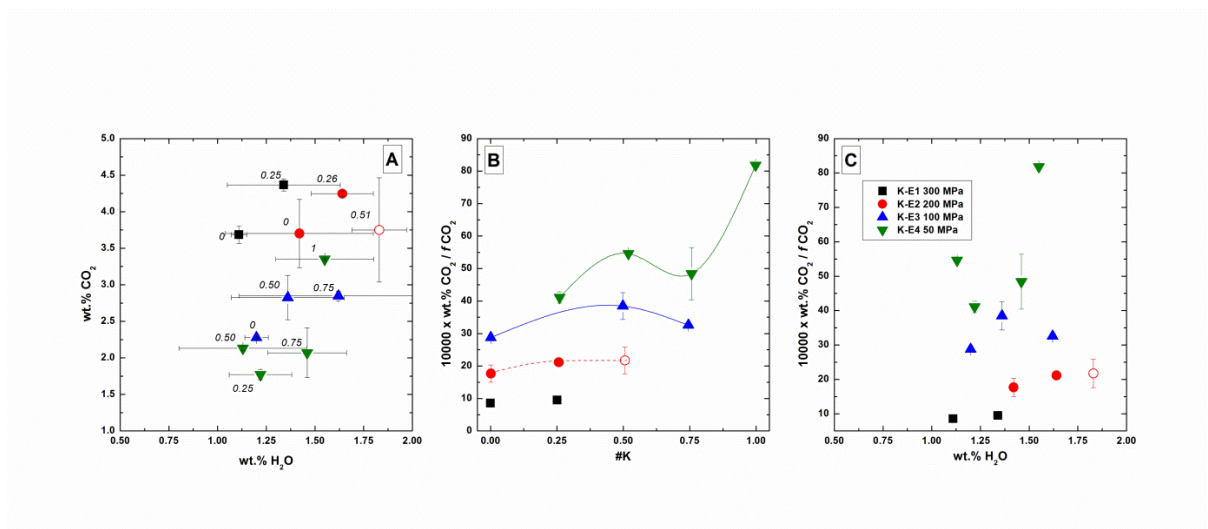


Figure 5. A) wt.% CO₂ as a function of wt.% H₂O. The #K is indicated next to each data point. B) wt.% CO₂ normalized to $f\text{CO}_2$ ($10000 \times \text{wt.}\% \text{CO}_2 / f\text{CO}_2$) showing the CO₂ thermodynamic activity as a function of #K. C) CO₂ activity ($10000 \times \text{wt.}\% \text{CO}_2 / f\text{CO}_2$) the as a function of the wt.% H₂O. The $f\text{CO}_2$ was calculated from the fluid phase composition ($X\text{CO}_2^{\text{fl}}$ in Table 2) and the standard $f^{\theta}\text{CO}_2$ from Holland and Powell (1991) such as $f\text{CO}_2 = X\text{CO}_2^{\text{fl}} \times f^{\theta}\text{CO}_2$. The open symbol corresponds to the CO₂ and H₂O contents determined for glass sample showing evidences of crystalline material (K10-E2 in Table 2).

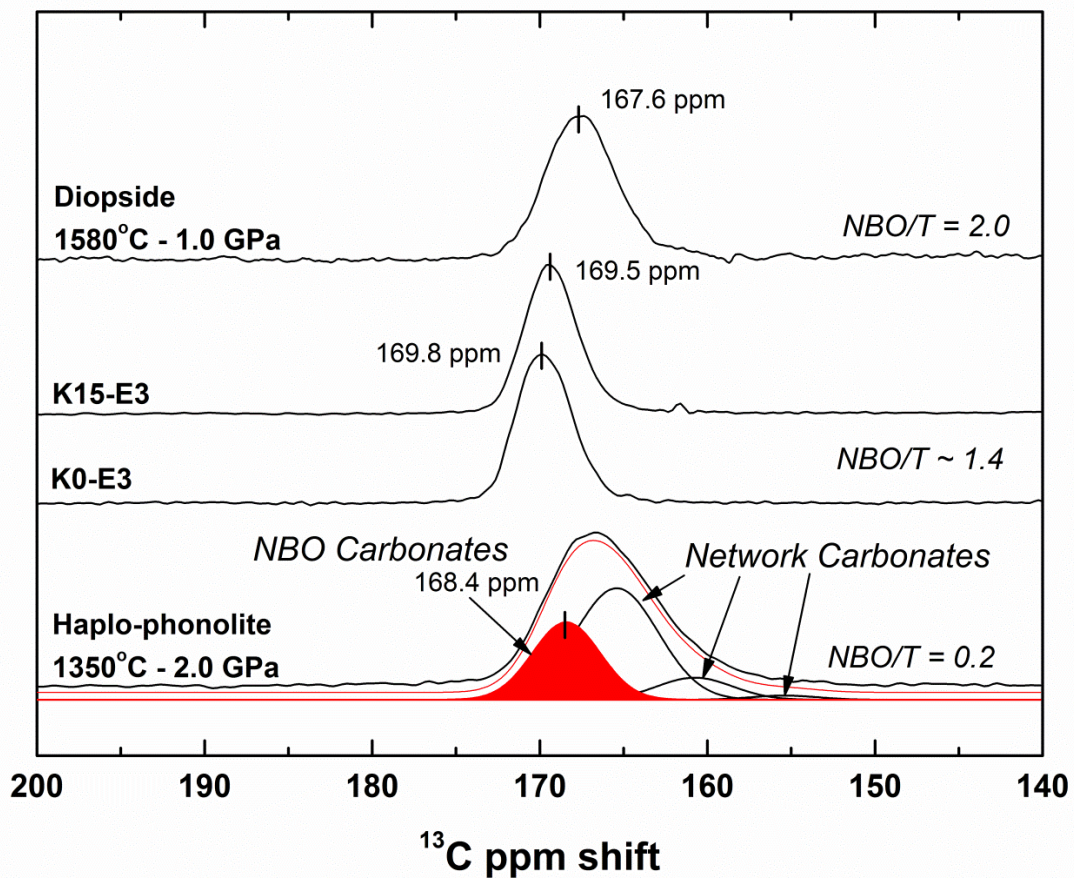


Figure 6. Comparison of ^{13}C MAS NMR spectra obtained for different compositions ranging from slightly depolymerized (haplo-phonolite with an $\text{NBO}/\text{T} = 0.2$ from Morizet et al., 2002) to highly depolymerized (diopside with an $\text{NBO}/\text{T} = 2$, from Morizet, 2002). ^{13}C spectra obtained for K0-E3 and K15-E3 are reported as a comparison. The haplo-phonolite spectrum simulation from Morizet et al. (2002) is shown. The comparison suggests that most of the carbonates if not all are dissolved as NBO-carb. $\text{M}^{\text{n}+}$ in K0-E3 and K15-E3. The charge compensating cation ($\text{M}^{\text{n}+}$) is likely to be Na^+ and/or K^+ , however, the actual NMR resolution does not allow deciphering the exact chemical shift of each individual species. .

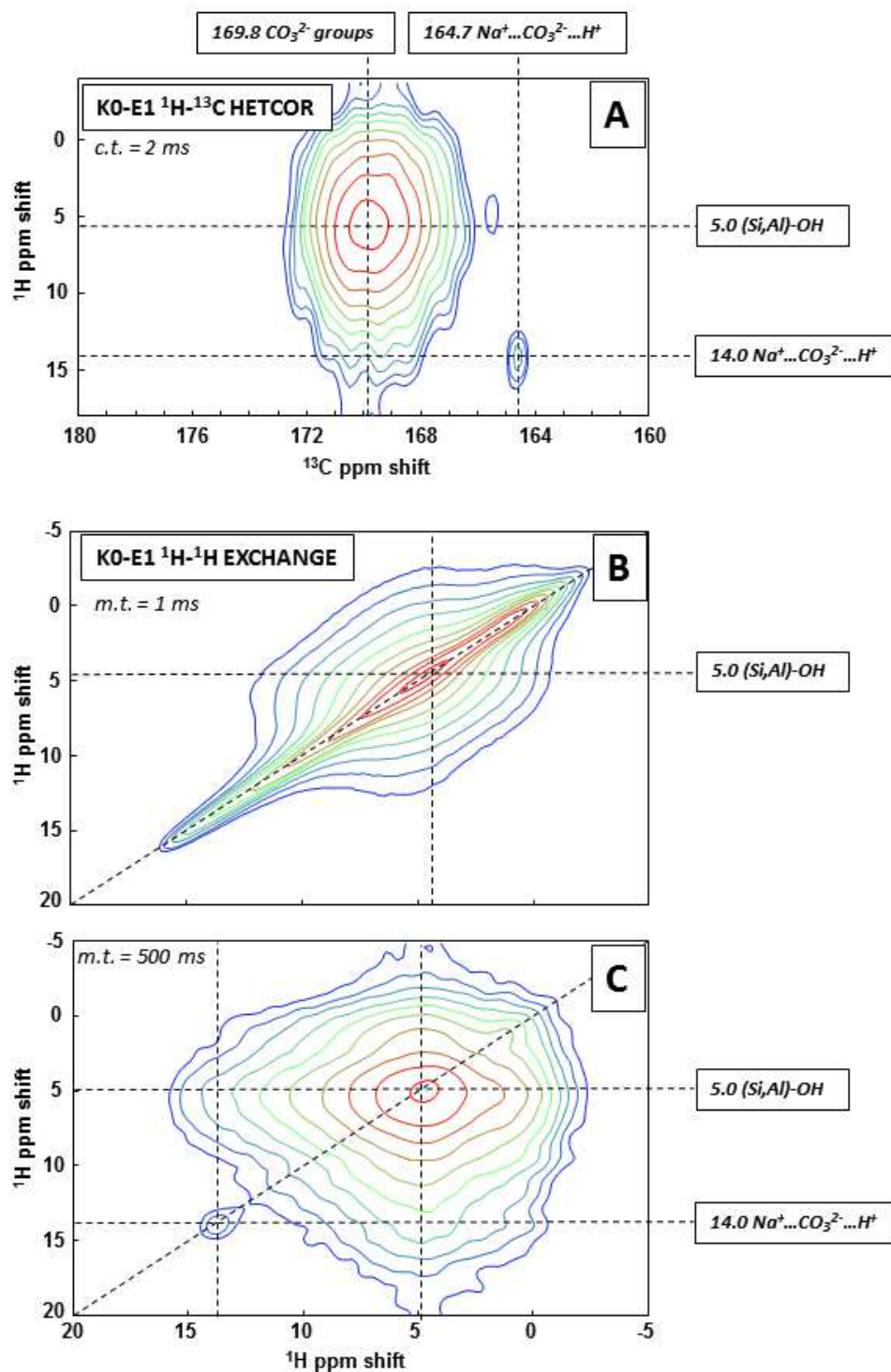


Figure 7. A) Acquired $\{^1\text{H}\}$ - ${}^{13}\text{C}$ HETCOR spectrum for K0-E1 glass synthesized at 300 MPa. The main CO_3^{2-} contribution at 169.8 ppm is correlated to a proton signature at 5.0 ppm corresponding to (Si,Al)-OH environments; the peak at 164.7 ppm corresponding to

isolated CO_3^{2-} environment is correlated to 14.0 ppm H environment. B) Homonuclear ^1H - ^1H EXCHANGE NMR spectrum acquired at 1 ms mixing time and C) Homonuclear ^1H - ^1H EXCHANGE NMR spectrum acquired at 500 ms mixing time. At 500 ms, the spin diffusion is effective for the main environments at +5.0 ppm associated to bonded hydroxyl in glass whereas the +14.0 ppm contribution remains on the diagonal in agreement with the isolated character of $\text{Na}^+ \dots \text{CO}_3^{2-} \dots \text{H}^+$ groups.

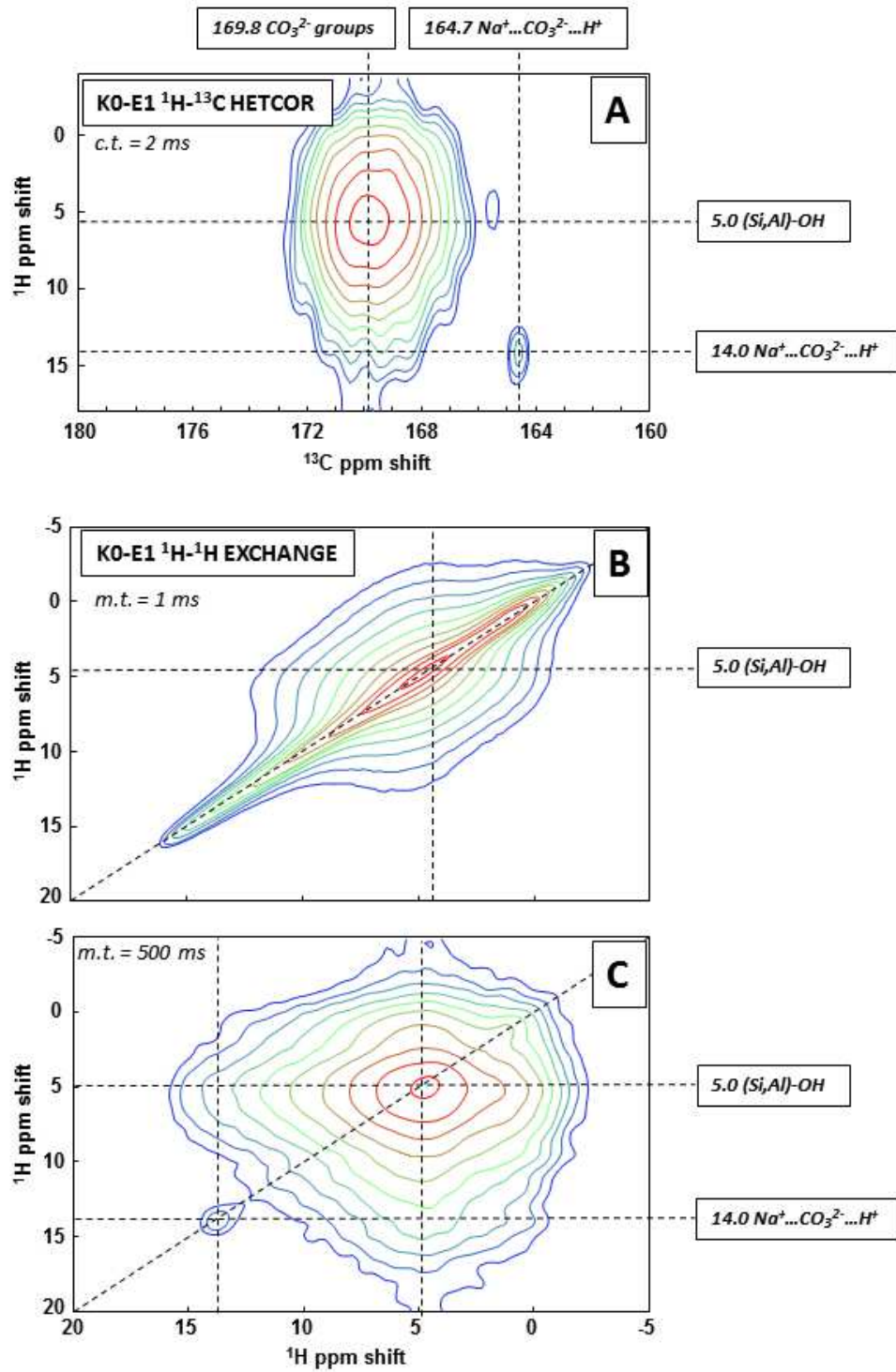


Table 1: Nephelinitic elemental compositions, synthetic compositions from this study and natural compositions

Oxides (mol.%) ^a	Theoretical composition in the present study					Nephelinitic compositions De Moor et al. (2013)	
	K0-E	K5-E	K10-E	K15-E	K20-E	Neph3_3	Neph1
SiO ₂	45	45	45	45	45	57.5	46.7
TiO ₂						0.6	1.9
Al ₂ O ₃	7	7	7	7	7	7.5	3.0
FeO						8.3	12.3
MgO	13	13	13	13	13	0.7	2.2
CaO	15	15	15	15	15	4.9	9.5
Na ₂ O	20	15	10	5	0	15.8	20.6
K ₂ O	0	5	10	15	20	4.8	3.7
Na ₂ O+K ₂ O	20	20	20	20	20	20.6	24.3
#K ^b	0	0.25	0.5	0.75	1	0.23	0.15
NBO/T ^c	1.39	1.39	1.39	1.39	1.39	0.74	1.67

^a The oxides concentrations are reported on a molar basis for the studied synthetic compositions (K0-E to K20-E) and for natural compositions (De Moor et al. (2013) and Mitchell and Dawson (2012)).

^b #K corresponds to the ratio $K_2O/(K_2O+Na_2O)$ on a molar basis.

^c The NBO/T is calculated following the method of Mysen (1988, 1990). It represents the ratio between the concentration of non-bridging oxygen (NBO) and tetrahedral cations (T). The NBO is calculated as the sum of the negative charges of the network modifier cations (Na^+ , K^+ , Mg^{2+} , Ca^{2+} and Fe^{2+}) and the Tetrahedral charges carried by the network former cations (Si^{4+} , Al^{3+} , Fe^{3+} and Ti^{4+}).

Table 2: Experimental conditions, glass elemental composition, dissolved volatile concentration and fluid phase composition.

Sample	K0-E1	K5-E1	K0-E2	K5-E2	K10-E2	K0-E3	K10-E3	K15-E3	K5-E4	K10-E4	K15-E4	K20-E4	K0-E5	K5-E5	K10-E5	K15-E5
T (°C)	125 0	115 0	115 0	115 0	115 0											
P (MPa)	308	308	209	209	209	117	117	117	56	56	56	56	106	106	106	106
Glass chemical composition (mol.%) ^a																
SiO ₂	47.4	47.8	46.4	46.6	46.6	48.8	47.1	48.1	47.2	47.5	47.7	46.6	47.1	47.0	47.0	47.1
Al ₂ O ₃	7.0	6.4	6.4	6.6	6.4	7.3	7.1	7.0	7.0	6.9	7.0	7.1	7.0	6.9	7.0	6.8
FeO	0.2	0.2	0.2	0.2	0.2	0.2	0.2	0.2	0.1	0.1	0.1	0.0	0.3	0.2	0.2	0.2
MgO	11.8	10.6	10.0	10.1	10.2	11.6	10.7	10.7	10.9	10.6	10.8	10.9	10.9	10.8	10.6	10.9
CaO	15.2	15.7	17.4	16.3	17.0	15.9	15.5	14.9	15.8	15.4	14.8	15.4	15.9	15.8	15.8	15.6
Na ₂ O	18.4	14.2	19.6	15.0	9.7	16.2	9.4	4.7	14.1	9.4	4.8	0.0	18.5	14.8	10.1	5.2
K ₂ O	0.0	5.0	0.0	5.2	10.0	0.0	9.9	14.4	5.0	10.1	14.8	20.0	0.2	4.5	9.3	14.1
EPMA shortfall (wt.%)	10.9	14.3	17.6	18.3	21.3	9.1	9.6	9.8	6.9	6.9	6.6	7.1	4.0	4.4	4.6	4.9
#K ^b	0.0	0.26	0.0	0.26	0.51	0.0	0.51	0.76	0.26	0.52	0.76	0.98	0.0	0.2	0.4	0.7
Al/(Al+ Si)	0.13	0.12	0.12	0.12	0.12	0.13	0.13	0.13	0.13	0.13	0.13	0.13	0.1	0.1	0.1	0.1
Ca/(Ca+ Mg)	0.56	0.60	0.64	0.62	0.62	0.58	0.59	0.58	0.59	0.59	0.58	0.59	0.5	0.5	0.6	0.5
Volatile content																
wt.% H ₂ O initial	3.15	2.88	5.41	5.56	5.96	4.18	5.01	3.76	2.80	3.47	3.03	3.81	3.2	2.9	3.0	3.3
wt.% H ₂ O dissolve d ^c	±0.0 4	±0.0 7	±0.3 8	±0.1 6	±0.1 4	±0.0 6	±0.2 9	±0.5 1	±0.1 6	±0.3 3	±0.2 0	±0.2 5	±0.2 28	±0.2 04	±0.2 16	±0.2 35
wt.% CO ₂ initial	13.8 7	13.8 7	13.8 7	13.8 7	14.6 2	13.8 7	14.6 2	13.8 7	13.8 7	14.6 2	13.8 7	13.8 7	0	0	0	0
CO ₃ /Q ⁿ	0.24	0.28	0.20	0.23	0.24	0.14	0.18	0.18	0.11	0.13	0.13	0.20				
HF Raman ratio	±0.0 08	±0.0 05	±0.0 30	±0.0 02	±0.0 47	±0.0 00	±0.0 20	±0.0 04	±0.0 05	±0.0 02	±0.0 22	±0.0 00	0	0	0	0
wt.% CO ₂ ^d	±0.1 2	±0.1 8	±0.4 7	±0.0 4	±0.7 1	±0.0 0	±0.3 0	±0.0 6	±0.0 7	±0.0 3	±0.3 4	±0.0 1	0	0	0	0
Fluid phase composition ^e																
X CO ₂ fluid	0.67	0.72	0.53	0.52	0.52	0.61	0.57	0.68	0.76	0.69	0.75	0.66	0	0	0	0
X H ₂ O fluid	0.33	0.28	0.47	0.48	0.48	0.39	0.43	0.32	0.24	0.31	0.25	0.34	1	1	1	1
fCO ₂ (bars) ^f	431 2	460 3	174 8	171 9	172 7	792	734	875	431	390	429	376	0	0	0	0

^a The glass composition was determined by EPMA analyses. The observed error based on replicated EPMA analyses associated to each oxide concentration is less 0.3 mol.% in relative at worse.

^b #K corresponds to the ratio K₂O/(K₂O+Na₂O) on a molar basis. The calculated error on each ratio is on the order of ± 0.01.

^c The wt.% H₂O was determined using Raman spectroscopy and following the method of Mercier et al. (2009) calibrated for a various range of bulk silicate glass composition.

^d The wt.% CO₂ was determined using Raman spectroscopy and using the method established by Morizet et al. (2013). The wt.% CO₂ is related to the determined CO₃/Qⁿ ratio from Raman spectra by a linear factor such as: wt.% CO₂ = 15.17 x CO₃/Qⁿ.

^e The fluid phase composition was calculated from mass balance calculations: $i^{\text{tot}} = i^{\text{fluid}} + i^{\text{glass}}$.

^fThe CO₂ fugacity (f_{CO_2}) was calculated from standard thermodynamic properties from Holland and Powell (1991).